



# Measuring and Replicating the 1–20 $\mu\text{m}$ Energy Distributions of the Coldest Brown Dwarfs: Rotating, Turbulent, and Nonadiabatic Atmospheres

S. K. Leggett<sup>1</sup>, Pascal Tremblin<sup>2</sup>, Mark W. Phillips<sup>3</sup>, Trent J. Dupuy<sup>4</sup>, Mark Marley<sup>5</sup>, Caroline Morley<sup>6</sup>,

Adam Schneider<sup>7,8</sup>, Dan Caselden<sup>9</sup>, Colin Guillaume<sup>9</sup>, and Sarah E. Logsdon<sup>10</sup>

<sup>1</sup> Gemini Observatory/NSF's NOIRLab, 670 N. A'ohoku Place, Hilo, HI 96720, USA; [sleggett@gemini.edu](mailto:sleggett@gemini.edu)

<sup>2</sup> Université Paris-Saclay, UVSQ, CNRS, CEA, Maison de la Simulation, F-91191, Gif-sur-Yvette, France

<sup>3</sup> University of Exeter, Stocker Road, Exeter EX4 4PY, UK

<sup>4</sup> Institute for Astronomy, University of Edinburgh, Royal Observatory, Blackford Hill, Edinburgh, EH9 3HJ, UK

<sup>5</sup> NASA Ames Research Center, Moffett Field, CA 94035, USA

<sup>6</sup> Department of Astronomy, University of Texas, Austin, TX 78712, USA

<sup>7</sup> US Naval Observatory, Flagstaff Station, P.O. Box 1149, Flagstaff, AZ 86002, USA

<sup>8</sup> Department of Physics and Astronomy, George Mason University, MS3F3, 4400 University Drive, Fairfax, VA 22030, USA

<sup>9</sup> Backyard Worlds: Planet 9, USA

<sup>10</sup> Kitt Peak National Observatory/NSF's NOIRLab, 950 North Cherry Avenue, Tucson, AZ 85719, USA

Received 2020 November 25; revised 2021 May 19; accepted 2021 June 9; published 2021 August 30

## Abstract

Cold, low-mass, field brown dwarfs are important for constraining the terminus of the stellar mass function, and also for optimizing atmospheric studies of exoplanets. In 2020 new model grids for such objects were made available: Sonora-Bobcat and ATMO 2020. Also, new candidate cold brown dwarfs were announced, and new spectroscopic observations at  $\lambda \approx 4.8 \mu\text{m}$  were published. In this paper we present new infrared photometry for some of the coldest brown dwarfs, and put the new data and models together to explore the properties of these objects. We reconfirm the importance of mixing in these atmospheres, which leads to CO and  $\text{NH}_3$  abundances that differ by orders of magnitude from chemical equilibrium values. We also demonstrate that the new models retain the known factor  $\gtrsim 3$  discrepancy with observations at  $2 \lesssim \lambda \mu\text{m} \lesssim 4$ , for brown dwarfs cooler than 600 K. We show that the entire  $1 \lesssim \lambda \mu\text{m} \lesssim 20$  energy distribution of six brown dwarfs with  $260 \leq T_{\text{eff}} \text{ K} \leq 475$  can be well reproduced, for the first time, by model atmospheres which include disequilibrium chemistry as well as a photospheric temperature gradient which deviates from the standard radiative/convective equilibrium value. This change to the pressure–temperature profile is not unexpected for rotating and turbulent atmospheres that are subject to diabatic processes. A limited grid of modified-adiabat model colors is generated, and used to estimate temperatures and metallicities for the currently known Y dwarfs. A compilation of the photometric data used here is given in Appendix C.

*Unified Astronomy Thesaurus concepts:* [Stellar convective zones \(301\)](#); [Infrared sources \(793\)](#); [Brown dwarfs \(185\)](#); [Stellar atmospheres \(1584\)](#)

*Supporting material:* data behind figures, machine-readable table

## 1. Introduction

Historically, the discovery of cooler main-sequence stars has led to tension between the observations and the synthetic spectral energy distributions (SEDs) generated by model atmospheres. Major advances are made with every discovery, which resolves most discrepancies, until the next coolest type is found. Plane-parallel, radiative-convective atmospheres in local thermodynamic and hydrostatic equilibrium did not reproduce observations of M dwarfs until more complete line lists of molecular transitions for hydrides and oxides were calculated (e.g., Allard & Hauschildt 1995; Cushing et al. 2003, 2005; Tennyson et al. 2007). Discovery of the very red L dwarfs led to the recognition of condensation and settling as important processes in cool atmospheres (Tsuji et al. 1996; Ruiz et al. 1997; Burrows & Sharp 1999; Lodders 1999; Ackerman & Marley 2001; Woitke & Helling 2003; Morley et al. 2012, 2014). Infrared observations provided evidence of additional nonequilibrium processes, with more CO absorption at  $\lambda \approx 4.5 \mu\text{m}$ , and less  $\text{NH}_3$  at  $\lambda \approx 1.5 \mu\text{m}$  and  $\lambda \approx 11 \mu\text{m}$  than would be present in an atmosphere in chemical equilibrium (e.g., Saumon et al. 2000, 2006; Leggett et al. 2007). Vertical transport of gas in the atmospheres of the solar system giant

planets produces nonequilibrium chemical abundances (Fegley & Prinn, R. G. 1985; Noll et al. 1997) and this became recognized as an intrinsic feature of cool stellar and substellar atmospheres also.

In the last decade, cold substellar objects have been discovered which have even more in common with the giant planets. Substellar objects, or brown dwarfs, have insufficient mass for stable fusion and they cool with time (Dantona & Mazzitelli 1985; Burrows & Liebert 1993; Baraffe et al. 1998; Saumon & Marley 2008; Phillips et al. 2020). These objects form the extended low-mass tail of the stellar mass function (e.g., Kirkpatrick et al. 2019, 2021), and brown dwarfs as low mass as 4 Jupiter masses have been found in young clusters and associations (Best et al. 2017; Esplin & Luhman 2017; Luhman & Hapich 2020; Lodieu et al. 2021). Older, free-floating, and cold very low-mass objects have also been found; the most extreme example is the few-gigayear-old WISE J085510.83-071442.5, hereafter, J0855, which is a 260 K,  $\sim 5$  Jupiter-mass object, 2 pc from the Sun (Luhman 2014; Luhman & Esplin 2016; Leggett et al. 2017). The properties of giant planets and brown dwarfs overlap significantly (Showman & Kaspi 2013; Morley et al. 2014; Line et al. 2015; Showman et al. 2019), and the difference between their formation

mechanisms is an active research area (Schlaufman 2018; Nielsen et al. 2019; Wagner et al. 2019; Bowler et al. 2020). The coldest objects have SEDs that are currently difficult to reproduce, and resolving this problem is important; characterization of the cold field brown dwarfs is vital for understanding both the terminus of the mass function and for optimizing studies of exoplanets. We tackle this problem here.

All but one of the known brown dwarf systems with effective temperature ( $T_{\text{eff}}$ )  $< 500$  K were discovered by the mid-infrared all-sky survey executed by the Wide-field Infrared Survey Explorer (WISE; Wright et al. 2010). The additional cold brown dwarf, a distant companion to the white dwarf WD 0806-661 (Luhman et al. 2011), was discovered in mid-infrared images taken by the Infrared Array Camera (IRAC; Fazio et al. 2004) on board the Spitzer Space Telescope (Werner et al. 2004). Some of these have been resolved into close similar-mass binary systems (e.g., Liu et al. 2011, 2012; Dupuy et al. 2015), while others appear super-luminous (compared to models) but have not been resolved in high spatial-resolution imaging (Beichman et al. 2013; Opitz et al. 2016).

Synthetic SEDs show that half of the energy emitted by a brown dwarf with  $T_{\text{eff}} < 600$  K is captured by the WISE W2 filter centered at  $\lambda \approx 4.6 \mu\text{m}$  (or the similar Spitzer [4.5] filter). In contrast, very little flux emerges through the W1 filter bandpass (or the Spitzer [3.6] filter), which includes the strong  $3.3 \mu\text{m}$   $\text{CH}_4$  absorption (e.g., Leggett et al. 2017). Hence, cold brown dwarfs can be identified by very red W1 – W2 (or [3.6] – [4.5]) colors. Currently  $\sim 50$  brown dwarfs with  $T_{\text{eff}} \lesssim 450$  K, classified as Y dwarfs, are known (Cushing et al. 2011, 2014; Luhman et al. 2011; Kirkpatrick et al. 2012, 2013; Tinney et al. 2012; Luhman 2014; Pinfield et al. 2014b; Schneider et al. 2015; Martin et al. 2018; Marocco et al. 2019; Bardalez Gagliuffi et al. 2020; Meisner et al. 2020a, 2020b). Based on spectral analyses of an early subset of these objects, Leggett et al. (2017) found that most are relatively young, lower-gravity, and lower-mass objects,  $\sim 1$ – $3$  Gyr old and  $\sim 6$  Jupiter-mass, but there were also a few older, higher-gravity, and higher-mass objects,  $\sim 6$  Gyr old and  $\sim 14$  Jupiter mass; a range of metallicity was also indicated. It is likely that the larger sample follows a similar distribution in age and metallicity as these values are typical of the low-mass solar neighborhood (Dupuy & Liu 2017; Buder et al. 2019).

In the year 2020, two new cold brown dwarf model grids were made available. One of these is the Sonora-Bobcat grid<sup>11</sup> of solar- and non-solar metallicity atmospheres, with the atmospheres in chemical equilibrium (Marley et al. 2021). The other is the ATMO 2020 grid<sup>12</sup> of solar-metallicity models both in chemical equilibrium and out of equilibrium with weak and strong mixing (Phillips et al. 2020). Also in 2020, new candidate  $T_{\text{eff}} < 400$  K brown dwarfs were announced (Bardalez Gagliuffi et al. 2020; Meisner et al. 2020a, 2020b; Kirkpatrick et al. 2021), and new ground-based spectroscopic observations at  $\lambda \approx 4.8 \mu\text{m}$  were published (Miles et al. 2020). A study of the cold planet-like brown dwarfs which includes the mid-infrared, and uses state-of-the-art model atmospheres, is now possible. Such a study is timely, given the scheduled 2021 launch of the James Webb Space Telescope (JWST) for which such objects will be prime targets.

We present new infrared photometric measurements of cold brown dwarfs in Section 2. In Section 3, we compare the observed colors of late-T and Y-type brown dwarfs to the synthetic colors generated by the new atmospheric models. We show that, while the models can reproduce much of the SED, large discrepancies remain. In Section 4, we describe possible missing physics in the current models, which impacts the pressure–temperature adiabatic profile of the atmospheres. We test adiabat-adjusted model atmospheres in Section 5 by comparing synthetic spectra and photometry to observations of seven brown dwarfs, at wavelengths of  $1$ – $20 \mu\text{m}$ . We show that a much improved fit can be obtained, and in Section 6 we use a grid of the adiabat-adjusted models to explore the properties of a larger sample of Y dwarfs. Our conclusions are given in Section 7. In the Appendices, we illustrate trends with temperature for JWST colors, provide a grid of colors generated by the adiabat-adjusted models, and give a compilation of the photometry used in this work.

## 2. New Photometry

### 2.1. Image Processing

The DRAGONS software package (Labrie et al. 2019) was used to reduce all the new imaging data obtained at the Gemini Observatory for this work. DRAGONS documentation is available at: <https://dragons.readthedocs.io/en/stable/>.

For Gemini’s infrared cameras, DRAGONS performs these initial steps: the nonlinearity correction is applied; counts are converted from data numbers to electrons; bad pixel masks are applied; and the read and Poisson noise is added to the FITS extension, which carries the variance information. Multiple dark observations are stacked to create a master dark. A master flat is created from multiple lamps-on and lamps-off observations; the flat is normalized and thresholded for out-of-range values.

Science data is divided by the appropriate flat field for the filter and read mode. The sky contribution is determined for each pointing using the images taken at other positions in the dither pattern. The sky is then subtracted from each science image. Point sources are detected in each image, and these are used to align and stack the data set for each object. Each sky-subtracted image in the stack is numerically scaled based on the background signal, by factors typically  $< 5\%$ , to produce a final image. For images obtained with the adaptive optics multi-detector imager Gemini South Adaptive Optics Imager (GSAOI) at Gemini South (McGregor et al. 2004), an add-on package called Disco-Stu determines the astrometric transformations to perform the stacking and create the final image.

We used simple aperture photometry to measure magnitudes from processed images. The processed images either came from our new Gemini observations or from data archives, as we describe below. We used circular apertures with annular sky regions positioned to avoid nearby sources. The size of the target aperture was typically small, with diameters of  $6$ – $10$  native pixels, in order to reduce noise and exclude potential nearby sources. We corrected for any loss of flux through the aperture by determining aperture corrections using bright isolated point sources in the science target image. Zero-points for the processed images were determined from calibrators in the image or observed separately, or from the FITS header in the case of archival data. Extinction corrections were not applied to the ground-based data because the near-infrared

<sup>11</sup> <https://zenodo.org/record/1405206#.XqoiBVNKiH4>

<sup>12</sup> <http://opendata.erc-atmo.eu>

extinction is small<sup>13</sup> and the targets were observed at airmasses  $\lesssim 1.7$ .

## 2.2. Gemini Observatory J-band Photometry of Candidate Cold Brown Dwarfs

To examine the nature of the candidate late-type brown dwarfs identified by Marocco et al. (2019) and Meisner et al. (2020a, 2020b), we obtained J-band imaging at Gemini Observatory using the Near-Infrared Imager (NIRI) at Gemini North (Hodapp et al. 2003) and FLAMINGOS-2 at Gemini South (Eikenberry et al. 2006). Table 1 gives target names and Gemini program identifications; the targets were selected as those accessible at the time of the Observatory’s Proposal Calls.

The J filter is defined by the Maunakea Observatories (MKO) photometric system (Tokunaga et al. 2002). The camera pixel scales are  $0.12''$  for NIRI and  $0.18''$  for FLAMINGOS-2. Telescope dithers of  $12''$ – $15''$  were used, in the form of a 5- or 9-point grid. All nights were photometric and the targets were observed at airmasses of 1.1–1.7. The delivered FWHM of the point-spread function (PSF) was  $0.4''$ – $1.0''$ . The magnitude zero-point was determined from the UKIRT Infrared Deep Sky Survey (UKIDSS) or Visible and Infrared Survey Telescope for Astronomy (VISTA) sky survey photometry (Lawrence et al. 2007; McMahon et al. 2013; Sutherland et al. 2015; Dye et al. 2018) of stars in the field of view; typically four to eight such stars were available. In the case of J094005.50+523359.2, hereafter J0940, only two survey stars were available and the zero-point was determined by averaging the value implied by those stars plus a measurement of a UKIRT Faint Standard (Leggett et al. 2006) executed immediately after the one-hour science observation and at a similar airmass (1.1 see 1.2 for the science); the three zero-point measurements agreed to 10%. Sky noise for these images was typically at the 5%–10% value, and usually dominated the uncertainty. Table 1 gives the final values.

One of the targets, CWISEP J021243.55+053147.2, hereafter J0212, was identified by Meisner et al. (2020a) as having very red  $[3.6] - [4.5]$  colors, but not having significant motion, and therefore not listed in their table of Y dwarf candidates. Subsequently, Kirkpatrick et al. (2021) also determined a low-significance motion of  $\mu_\alpha = -59.8 \pm 45.0$  and  $\mu_\delta = 57.0 \pm 27.4$  mas yr<sup>−1</sup>, as well as a poor-quality parallax of  $24.7 \pm 16.3$  mas—Kirkpatrick et al. (2021) suggest that J0212 is a background source. However, the extremely red  $J - [4.5]$  color that we measure for this object, with very little flux at  $[3.6]$ , implies that J0212 is cold and molecule-rich. The study of WISE colors by Nikutta et al. (2014) shows that AGN and infrared luminous galaxies can be very red in  $W1 - W2$ , however such objects are also red in  $W2 - W3$ ; if J0212 falls into such a category it would be detected in  $W3$ , which it is not. A more plausible solution is that the object is a binary and the actual parallax value is close to the upper limit of the current measurement; we show below that the luminosity of J0212 is then consistent with the observed  $J - [4.5]$  and  $[3.6] - [4.5]$  colors. We therefore suggest that J0212 is a binary Y dwarf at a distance of  $\sim 24$  pc.

## 2.3. Other New Near-infrared Photometry

As part of a project to measure photometric transformations between the UKIDSS and VISTA sky survey, NIRI, and FLAMINGOS-2 systems, a field containing the Y dwarf WISE J033605.05-014350.4 was observed at Gemini North at  $YJHK_{sK}$  (the brown dwarf was not detected at  $K$ ), and a field containing the Y dwarf CWISEP J093852.89+063440.6 was observed at Gemini South at  $JHK_s$ . The data were reduced in the manner described in the previous section, and the results are given in Table 1.

Table 1 lists the  $JH$  magnitudes for WISEA J050615.56-514521.3, which was listed by Meisner et al. (2020b) as a very late-T dwarf candidate. This object was also targeted in the deep WISE search by Pinfield et al. (2014a) and the unpublished photometry and spectral type (from their spectroscopy) is provided courtesy of a private communication with that team.

We measured  $YJHK$  magnitudes for the late-T subdwarf WISE J200520.38+542433.9, also known as Wolf 1130C (Mace et al. 2013a), in order to have a set of near-infrared colors for a known very metal-poor object with  $[m/H] \approx -0.75$  (Kesseli et al. 2019). The data were obtained using NIRI at Gemini North and were reduced in the manner described in the previous section. The results are given in Table 1.

CWISE J092503.20-472013.8 was listed by Kirkpatrick et al. (2021) as a candidate Y0 dwarf based on its motion, and  $W1 - W2$  color ( $3.93 \pm 0.38$ ). We used VVVX ESO Public Survey data<sup>14</sup> to determine the  $J$  magnitude given in Table 1. The brown dwarf was not detected in the  $K_s$  survey data. The  $J - W2$  color of the target ( $2.99 \pm 0.06$ ) provides an improved spectral type estimate of T8, based on Figures 13 and 14 of Kirkpatrick et al. (2021).

In addition, we searched for detections in the UKIDSS and VISTA surveys’ imaging data for Y dwarfs without near-infrared photometry. We determined magnitudes for two Y0 dwarfs from the VISTA Hemisphere Survey (VHS; McMahon et al. 2013): WISEA J030237.53-581740.3 ( $J$ ), and WISEA J224319.56-145857.3 ( $Y, J$ ). The results are given in Table 1.

Finally, to explore the known discrepancy between observations and models at  $\lambda \approx 2 \mu\text{m}$  (e.g., Leggett et al. 2019), we obtained  $K$ -band images of the Y1 dwarf WISE J064723.23-623235.5 (Kirkpatrick et al. 2013), hereafter J0647. This object was chosen in order to better measure the discrepancy for the coldest Y dwarfs, where little  $K$ -band imaging is available. Because of the faintness of the target, we used the adaptive optics imager GSAOI (McGregor et al. 2004) at Gemini South. Table 1 gives the program identification and the dates on which J0647 was observed. The imager has a pixel scale of  $0.02''$ . The nights were photometric and the delivered FWHM was  $\sim 0.1''$ . Sixty-six 90 s observations were made, of which 52 with better seeing of  $\leq 0.095''$  were used in the final image. J0647 was observed at an airmass of  $\sim 1.2$ , and the telescope was dithered by random  $1''$ – $4''$  offsets. Aperture photometry was carried out with apertures of diameter  $0.12''$  and  $0.20''$ , which gave consistent results after the application of the aperture corrections. The magnitude zero-point was determined using stars from the VISTA Hemisphere Survey (McMahon et al. 2013) which were in the GSAOI field of view. Table 1 gives our derived  $K_s$  for J0647.

<sup>13</sup> <https://www.gemini.edu/observing/telescopes-and-sites/sites>

<sup>14</sup> <https://www.eso.org/sci/publications/announcements/sciann17186.html>

**Table 1**  
New Near-infrared Photometry and Estimates of  $T_{\text{eff}}$

WISE Name R.A./Decl. $J$	Discovery Ref.	Spec. Type	Type Ref.	Gemini Program ID	Obs. Date yyyymmdd	Instrument Name	On-source Exp., hr	Photometry, MKO mag					$T_{\text{eff}}$ K	
								$Y$	$J$	$H$	$K_s^a$	$K$	Est.	Ref.
021243.55 +053147.2	Me20a	Y1	1	GS-2019B-DD-107	20191211	FLAMINGOS-2	1.38		22.70 $\pm 0.09$				390	2
030237.53 −581740.3	Ti18	Y0:	Ti18		2013	VIRCAM <sup>b</sup>			20.67 $\pm 0.23$				460	2
032109.59 +693204.5	Me20a	Y0.5	Me20a	GN-2020B-Q-321	2020 Sep 30	NIRI	0.58		21.30 $\pm 0.06$				415	2
033605.05 −014350.4	Ma13b	Y0	Ma18	GN-2020B-ENG-1	2020 Oct 1	NIRI	0.57	21.02 <sup>c</sup> $\pm 0.11$	21.26 $\pm 0.14$	21.59 $\pm 0.31$	21.4 $\pm 0.5$		445	2
040235.55 −265145.4	Me20a	Y1	Me20a	GS-2021A-FT-205	2021 Mar 22	FLAMINGOS-2	0.8		24.0 $\pm 0.5$				370	2
050305.68 −564834.0	Me20b	Y1	Me20b	GS-2021A-FT-205	2021 Mar 3	FLAMINGOS-2	2.11		22.54 $\pm 0.09$				345	2
050615.56 −514521.3	Me20b	T8	PGpc	GS-2013B-Q-16	2013 Dec 24	FLAMINGOS-2	0.16		20.31 $\pm 0.05$	20.89 $\pm 0.14$			600	1
064723.23 −623235.5	Ki13	Y1	Ki13	GS-2019B-Q-220	2012 Dec 10, 12, 13, 14	GSAOI	1.30				23.03 $\pm 0.15$		405	2
085938.95 +534908.7	Me20a	Y0	Me20a	GN-2020B-Q-321	2020 Dec 25	NIRI	0.13		21.39 $\pm 0.15$				450	2
092503.2 −472013.8	Ki21	T8	1		2017	VIRCAM <sup>d</sup>			18.29 $\pm 0.05$				700	1
093852.89 +063440.6	Me20a	Y0	Me20a	GS-CAL20210429	2021 Apr 29	FLAMINGOS-2	0.44		21.08 0.10	21.49 0.21	21.11 0.23		455	2
094005.50 +523359.2	Me20a	$\geq Y1$	Me20a	GN-2020A-FT-205	2020 Mar 10	NIRI	0.88		21.88 $\pm 0.11$				410	2
125721.01 +715349.3	Me20b	Y1	Me20b	GN-2021A-FT-206	2021 Apr 9	NIRI	1.72		23.35 $\pm 0.20$				390	2
144606.62 −231717.8	Me20a	$\geq Y1$	Me20a	GS-2020A-FT-204	2020 Mar 5	FLAMINGOS-2	4.32		23.20 $\pm 0.14$				350	2
193054.55 −205949.4	Me20b	$\geq Y1$	Me20b	GN-2020B-Q-321	2020 Oct 1	NIRI	1.78		22.54 $\pm 0.13$				365	2
193518.58 −154620.3	Ma19	$\geq Y1$	Me20a	GN-2020B-Q-321	2020 Aug 23 Sep 29, 30	NIRI	1.70		23.93 $\pm 0.33$				365 <sup>e</sup>	2
193656.08	Me20a	Y0	Me20a	GN-2020B-Q-321	2020 Oct 1	NIRI	0.03		20.16				450	2

4

**Table 1**  
(Continued)

WISE Name R.A./Decl. <i>J</i>	Discovery Ref.	Spec. Type	Type Ref.	Gemini Program ID	Obs. Date yyyymmdd	Instrument Name	On-source Exp., hr	Photometry, MKO mag					$T_{\text{eff}}$ K	
								<i>Y</i>	<i>J</i>	<i>H</i>	$K_s^a$	<i>K</i>	Est.	Ref.
+040801.2									$\pm 0.12$					
200520.38	Ma13a	sdT8	Ma13a	GN-2021A-FT-206	2021 May 11	NIRI	1.4	19.99 <sup>f</sup>	19.54	19.55		21.00	600	1
+542433.9					May 17			0.07	0.07	0.03		0.09		
223022.60	Me20a	$\geq Y1$	Me20a	GN-2020B-Q-321	2020 Oct 1, 5	NIRI	1.30		22.99				395	2
+254907.5									$\pm 0.20$					
224319.56	Me20b	Y0	Me20b		2013	VIRCAM <sup>b</sup>		21.16	21.14				450	2
-145857.3								$\pm 0.34$	$\pm 0.26$					
224916.17	Me20a	T9.5	Me20a	GN-2020B-Q-321	2020 Sep 17	NIRI	0.28		21.89				460	2
+371551.4									$\pm 0.10$					

**Notes.**

<sup>a</sup> Leggett et al. (2015) measure  $K - K_s = 0.4 \pm 0.1$  for a T8 and a T9 dwarf using FLAMINGOS-2, implying  $K = 21.8 \pm 0.5$  for J033605.05-014350.4,  $K = 23.43 \pm 0.18$  for J064723.23-623235.5, and  $K = 21.51 \pm 0.25$  for J093852.89+063440.6.

<sup>b</sup> Measured here using VISTA VHS imaging data.

<sup>c</sup> In the native NIRI system  $Y = 21.19 \pm 0.10$  for J033605.05-014350.4; we adopted  $Y_{\text{NIRI}} - Y_{\text{MKO}} = 0.17 \pm 0.03$  as determined by Liu et al. (2012) for late-T and Y dwarfs.

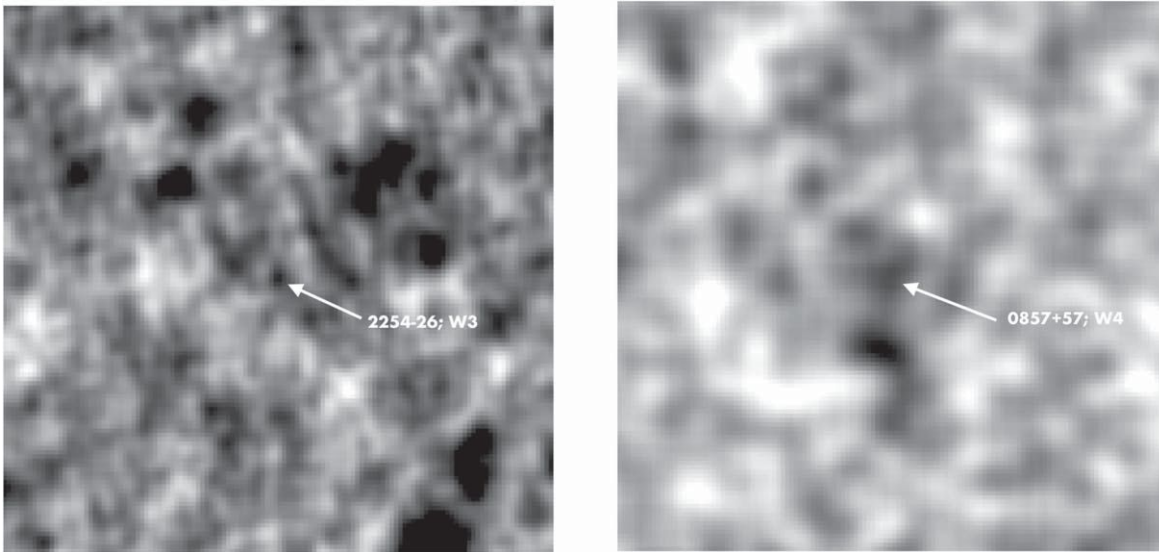
<sup>d</sup> Measured here using VVVX ESO Public Survey imaging data.

<sup>e</sup> Assuming the system is an equal-mass binary, see Section 6.3.

<sup>f</sup> In the native NIRI system  $Y = 20.03 \pm 0.05$  for J200520.38-145857.3; we synthesized  $Y_{\text{NIRI}} - Y_{\text{MKO}}$  for this object using the observed *Y*-band spectrum from Mace et al. (2013a) and the filter profiles for NIRI (<https://www.gemini.edu/instrumentation/niri/components#Filters>) and MKO (<http://svo2.cab.inta-csic.es/theory/fps/index.php?id=UKIRT/UKIDSS.Y&&mode=browse&gname=UKIRT&gname2=UKIDSS#filter>).

**References.** (1) this work, type ( $\pm \approx 0.5$ ) based on the type color, and  $T_{\text{eff}}$  ( $\pm \approx 50$  K) based on the  $T_{\text{eff}}$ -color, relationships of Kirkpatrick et al. (2019, 2021), (2) this work,  $T_{\text{eff}}$  ( $\pm \approx 25$  K) based on the  $T_{\text{eff}}$ -color relationships determined in Section 6.2, with  $T_{\text{eff}}$  values rounded to 5 K; Ki13—Kirkpatrick et al. (2013), Ki21—Kirkpatrick et al. (2021), Ma13a—Mace et al. (2013a), Ma13b—Mace et al. (2013b), Ma18—Martin et al. (2018), Ma19—Marocco et al. 2019, Me20a, b—Meisner et al. (2020a, 2020b), PGpc—P. Pinfield and M. Gromadzki, private communication 2014; Ti18—Tinney et al. (2018).





**Figure 1.** Examples of WISE images where faint brown dwarfs were previously not included in the ALLWISE catalog (left) or where the photometry was compromised by background sources (right). In the latter case, the smaller aperture used here allowed the brown dwarf to be better isolated, resulting in a W4 magnitude fainter than the catalog value by  $\sim 2$  mag.

#### 2.4. Mid-infrared Photometry

Our goal is to reproduce the SED of the coldest brown dwarfs over all wavelengths where significant flux is emitted. It is important therefore to include the mid-infrared region; furthermore, knowledge of the mid-infrared is crucial for planning observations with JWST.

WISE catalog photometry<sup>15</sup> of faint targets can be compromised by nearby objects, and fainter objects are sometimes omitted altogether. The sensitivity limits for a signal-to-noise ratio (S/N) = 5 are  $\sim 11.5$  and  $8.0$  magnitudes for the W3 ( $\lambda \sim 14 \mu\text{m}$ ) and W4 ( $\lambda \sim 22 \mu\text{m}$ ) filters, respectively.<sup>16</sup> We examined the W3 and W4 images provided by the WISE Image Service<sup>17</sup> for the colder brown dwarfs, and determined new or revised values for the photometry based on this visual inspection. We also looked for W3 and W4 data for warmer brown dwarfs to determine color trends. We identified sources where a point source could be resolved by eye, at the correct location for the epoch of the W3 or W4 observation, allowing for the proper motion of the source. Figure 1 gives examples of sky regions where we obtained new or revised WISE magnitudes.

We carried out aperture photometry on the WISE images using apertures of 3 or 5 pixel radii ( $4''$  or  $7''$ ) and annular skies. These apertures are smaller than the predefined fitting radius used by the ALLWISE profile-fitting photometry routine,  $r_{\text{fit}}$ :  $r_{\text{fit}} = 1.25 \times \text{FWHM}$  where FWHM is  $6''$  for bands 1–3 and  $12''$  for band 4<sup>18</sup>. The smaller aperture reduced the noise contribution from the background and improved exclusion of nearby sources. Aperture corrections were measured using isolated and brighter stars in the field. Zero-points are taken from the WISE image header. Table 2 gives our new W3 and W4 measurements, as well as the ALLWISE Source Catalog values. The uncertainties in the new measurements are due to

background noise and are large in most cases, with S/Ns of 2 or 3 only. Nevertheless significant differences exist between our values and those reported in the catalog (Table 2). These long-wavelength colors are useful for comparing to colors generated by current model atmospheres, and for planning JWST observations.

CWISE J112106.36-623221.5 was listed by Kirkpatrick et al. (2021) as a candidate Y0 dwarf, based on its motion, W2 detection and W1 non-detection. Spitzer imaging data are available for the source via AORs r42735360 and r23699712 at the Spitzer Heritage Archive.<sup>19</sup> We carried out aperture photometry on these images using apertures of 3 pixel radii ( $1.8''$ ) and annular skies. Aperture corrections were measured using isolated and brighter stars in the field, and the counts calibrated photometrically according to the Spitzer IRAC Manual<sup>20</sup>. Table 2 gives the [3.6] and [4.5] magnitudes for the source, which was not detected at longer wavelengths in the earlier cryogenic observation. The two measurements of the source, taken four years apart, agree to 20% at [3.6] and 2% at [4.5]. The [3.6] – [4.5] color of the target ( $1.34 \pm 0.11$ ) provides an improved spectral type estimate of T7, based on Figure 14 of Kirkpatrick et al. (2021).

### 3. Observed and Modeled Colors of T and Y Dwarfs

Models of brown dwarf atmospheres are typically characterized by a set of physical and chemical parameters. The most fundamental is the total energy output, or luminosity ( $L$ ) which is defined by Stefan’s law as  $L = \sigma T_{\text{eff}}^4 \times 4\pi R^2$ , where  $\sigma$  is the Stefan–Boltzmann constant,  $R$  is the radius of the object, and  $T_{\text{eff}}$  the effective temperature. Another important parameter is the surface gravity  $g$ , which is defined as  $g = GM/R^2$ , where  $M$  is the mass and  $G$  is the gravitational constant. The chemical composition of the atmosphere is usually described as the abundance of metals relative to hydrogen [m/H], normalized to the solar value. In addition, some models include cloud

<sup>15</sup> <https://irsa.ipac.caltech.edu/cgi-bin/Gator/nph-dd>

<sup>16</sup> [https://wise2.ipac.caltech.edu/docs/release/allwise/expsup/sec2\\_3a.html](https://wise2.ipac.caltech.edu/docs/release/allwise/expsup/sec2_3a.html)

<sup>17</sup> <https://irsa.ipac.caltech.edu/applications/wise/>

<sup>18</sup> [https://wise2.ipac.caltech.edu/docs/release/allsky/expsup/sec4\\_4c.html#wpro](https://wise2.ipac.caltech.edu/docs/release/allsky/expsup/sec4_4c.html#wpro)

<sup>19</sup> <https://sha.ipac.caltech.edu/applications/Spitzer/SHA/>

<sup>20</sup> [https://irsa.ipac.caltech.edu/data/SPITZER/docs/irac/iracinstrumenthandbook/14/#\\_Toc59022361](https://irsa.ipac.caltech.edu/data/SPITZER/docs/irac/iracinstrumenthandbook/14/#_Toc59022361)

**Table 2**  
Revised and New WISE and Spitzer Photometry

WISE Name R.A./Decl. <i>J</i>	Discovery Ref.	Spec. Type	Type Ref.	ALLWISE Catalog		This Work			
				W3	W4	W3	W4	[3.6]	[4.5]
001449.96+795116.1	Ba20	T8	Ba20			13.69 ± 0.40			
002810.59+521853.1	Me20b	T7.5	Me20b			13.95 ± 0.43			
013217.78–581825.9	Me20b	T9	Me20b			14.10 ± 0.41			
014603.23–261908.7	Me20b	T7.5	Me20b			13.63 ± 0.34			
081117.81–805141.3	Ma13b	T9.5	Ma13b	12.64 ± 0.32	9.21 ± 0.38		11.09 ± 0.65		
085510.83–071442.5 <sup>a</sup>	Lu14	>Y4	Ki19	11.14 ± 0.13		11.51 ± 0.06	10.56 ± 0.50		
085757.95+570847.5	Ge02	L8	Ge02	10.32 ± 0.06	8.64 ± 0.35		10.48 ± 0.50		
093735.63+293127.2	Bu02	T6pec	Bu06	10.70 ± 0.10			10.36 ± 0.34		
105349.41–460241.2	Me20b	T8.5	Me20b			14.13 ± 0.40			
112106.36–623221.5	Ki21	T7	1					16.47 ± 0.10	15.13 ± 0.04
125721.01+715349.3	Me20b	Y1	Me20b			13.55 ± 0.33			
182831.08+265037.8	Cu11	>Y2	Ki12	12.44 ± 0.34			10.65 ± 0.52		
193054.55–205949.4	Me20b	Y1	Me20b			14.44 ± 0.58			
214025.23–332707.4	Me20b	T8.5	Me20b			13.32 ± 0.32			
225404.16–265257.5	Me20b	T9.5	Me20b			13.29 ± 0.29			

**Note.**

<sup>a</sup> Wright et al. (2014) and Kirkpatrick et al. (2019) demonstrate that the first epoch of WISE observations of J0855 are significantly contaminated at W1 by background sources. The W3 and W4 images date to the same epoch and the background sources will therefore be at the same location as J0855. Wright et al. (2014) measure  $W1 = 16.12$  and  $W1 - W2 = 0.67 \pm 0.17$  for these sources from images where J0855 has moved away (post-cryo). Nikutta et al. (2014) analyze WISE colors for large samples of Galactic sources; their Figure 6 (panel 3) shows that the  $W1 - W2$  color is likely to be on the bluer side of the Wright et al. (2014) measurement, and the most likely values of  $W2 - W3$  and  $W3 - W4$  are  $\sim 0.8$  and  $\sim 1.0$  respectively. Hence the background sources are expected to have  $W3 \approx 15$  and  $W4 \approx 14$ , and so are not likely to significantly contaminate the J0855 W3 and W4 values in the Table. The successful model fits we show in Section 5.2 support this conclusion.

**References.** (1) this work; Ba20—Bardalez Gagliuffi et al. (2020), Bu02—Burgasser et al. (2002), Bu06—Burgasser et al. (2006), Cu11—Cushing et al. (2011), Ge02—Geballe et al. (2002), Ki12—Kirkpatrick et al. (2012), Ki19—Kirkpatrick et al. (2019), Ki21—Kirkpatrick et al. (2021), Lu14—Luhman (2014), Ma13b—Mace et al. (2013b), Me20b—Meisner et al. (2020b).

formation via a sedimentation parameter and a fractional cloud cover (e.g., Morley et al. 2014). Also, some models represent vertical transport of gas (which results in disequilibrium chemical abundances) as a diffusive process, via the vertical eddy diffusivity parameter  $K_{zz}$  (square centimeters per second, e.g., Saumon et al. 2006). The models we use here are parameterized by  $T_{\text{eff}}$ ,  $g$ ,  $[\text{m}/\text{H}]$  and  $K_{zz}$ . They are cloud-free and we discuss the possible impact of clouds later in this paper.

Figures 2 and 3 show color–color and color–magnitude diagrams for late-T and Y-type brown dwarfs. Observed colors are plotted, as well as sequences from the Sonora-Bobcat models<sup>21</sup> (Marley et al. 2017, 2021) and the ATMO 2020 models<sup>22</sup> (Phillips et al. 2020).

Figure 2 shows various colors plotted against  $J - [4.5]$ , as a proxy for  $T_{\text{eff}}$ . Note however that  $J - [4.5]$  is also sensitive to gravity, metallicity, mixing, and clouds (e.g., Figure 3 bottom panel). The photometry is taken from this work (Tables 1 and 2) and the literature (Leggett et al. 2017; Kirkpatrick et al. 2019, 2021; Marocco et al. 2019, 2020; Bardalez Gagliuffi et al. 2020; Faherty et al. 2020; Meisner et al. 2020a, 2020b, see also the photometry compilation in Appendix C). Figure 3 shows color–magnitude diagrams for late-T and Y dwarfs with measured trigonometric parallaxes. Parallaxes are taken from Leggett et al. (2017), Martin et al. (2018), Kirkpatrick et al. (2019, 2021), Bardalez Gagliuffi et al. (2020), Marocco et al. (2020). The absolute [4.5] magnitude is shown as a function of the near-infrared color  $J - H$ , the mid-infrared color  $[3.6] - [4.5]$ , and the long-baseline color  $J - [4.5]$ . The absolute [4.5] magnitude can be used as a proxy for luminosity because  $\sim$ half

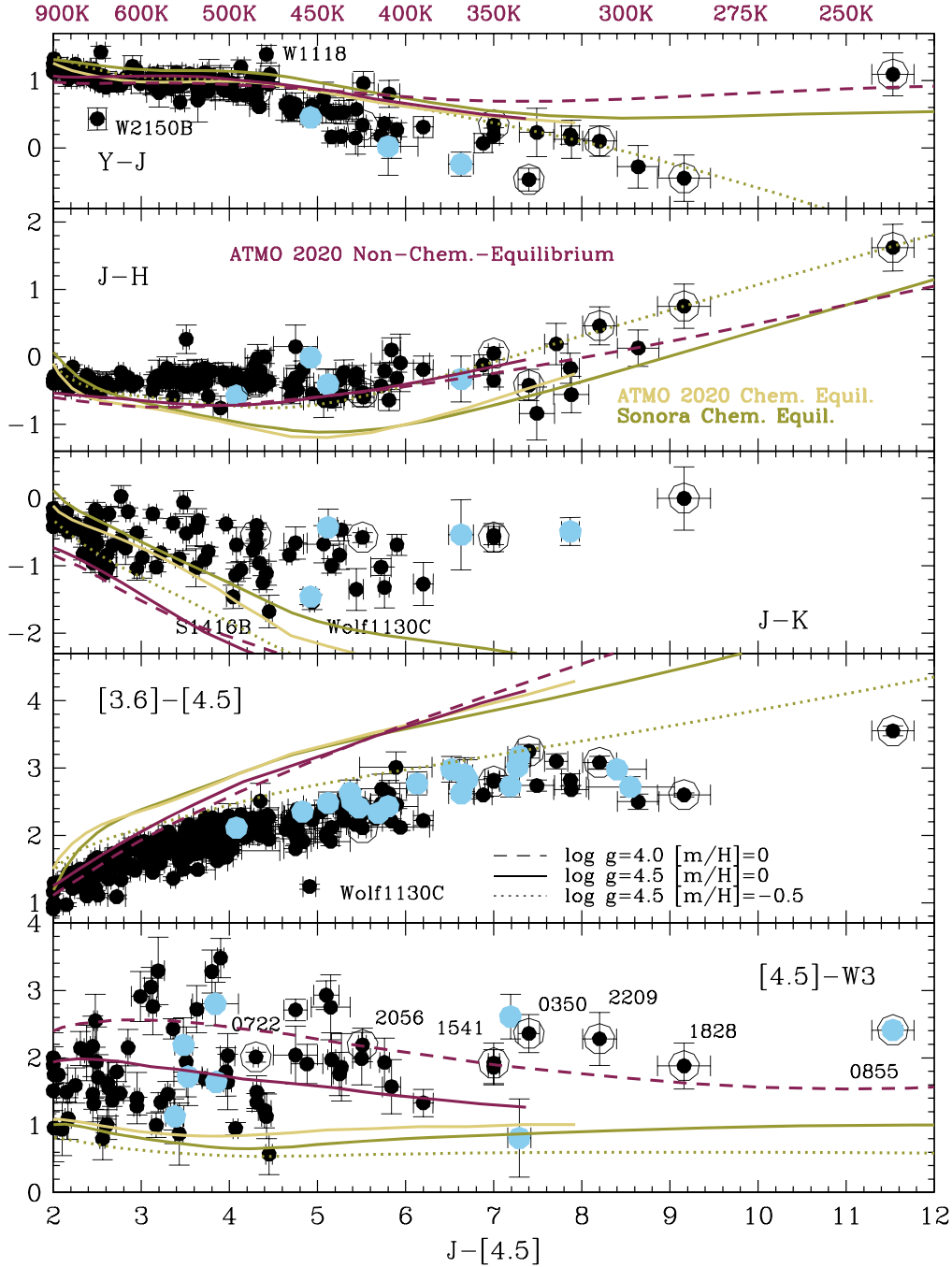
of the total energy is captured by this filter for cold brown dwarfs. Luminosity in turn is strongly correlated with  $T_{\text{eff}}$  through the Stefan–Boltzmann law, because the radius of a brown dwarf does not change significantly after around 0.3 Gyr (Burrows et al. 1997, see also Section 5.5). Note however that the [4.5] flux is also sensitive to gravity, metallicity, and mixing (e.g., Figure 3 bottom panel).

The new photometric measurements presented here (Tables 1 and 2) are represented by blue points in Figures 2 and 3. The new data support and build on the empirical sequence in each panel of Figure 2; the  $K$ -band data point for J0647 nicely fills in a gap in the  $J - K$  sequence at  $J - [4.5] \approx 8$ , and the new  $J$ -band data improves the definition of the tight  $J - [4.5]:[3.6] - [4.5]$  observational sequence. For the 400–600 K brown dwarfs, the  $J - K$  and  $[4.5] - W3$  colors appear to have a large degree of intrinsic scatter; we discuss this further in Section 6.2.

Figures 2 and 3 show that the most recent models at the time of writing, the ATMO 2020 and Sonora-Bobcat models, generate very similar colors for the same parameters. That is, the chemical equilibrium solar-metallicity cloud-free ATMO 2020 and Sonora-Bobcat model sequences (yellow and olive green solid lines in the figures) are very similar. The models, which include vigorous mixing (dark red lines), do a better job of reproducing the observed  $J - [4.5]:J - H$  and  $J - [4.5]:[4.5] - W3$  sequences in Figure 2, and the  $J - H:M_{[4.5]}$  and  $[3.6] - [4.5]:M_{[4.5]}$  sequences in Figure 3. This is because mixing in these cool atmospheres has the net result of decreasing the  $\text{NH}_3$  abundance and increasing  $\text{N}_2$ , and increasing CO at the expense of  $\text{CH}_4$  (e.g., Noll et al. 1997; Saumon et al. 2006, 2007; Visscher & Moses 2011; Zahnle & Marley 2014; Leggett et al. 2015; Tremblin et al. 2015; Phillips et al. 2020). The  $H$  and  $W3$

<sup>21</sup> <https://zenodo.org/record/1405206#.XqoiBVNKiH4>

<sup>22</sup> <http://opendata.erc-atmo.eu>



**Figure 2.** Color-color diagrams for late-T and Y dwarfs. Black dots are photometry from the literature; blue dots are new data presented here. Olive green lines are chemical equilibrium Sonora-Bobcat models, and yellow lines are chemical equilibrium ATMO 2020 sequences for a mass of  $0.015 M_{\odot}$  ( $\log g \approx 4.5$ ) and  $0.005 M_{\odot}$  ( $\log g \approx 4.0$ ). Line types indicate gravity and metallicity as in the legend. Approximate  $T_{\text{eff}}$  values along the top axis are from the ATMO 2020 nonequilibrium chemistry models. Circled points indicate seven dwarfs that we analyze in detail in Section 5, which are identified by short name in the bottom panel. Four color outliers are also identified: ULAS J141623.94+134836.30 (“S1416B”), WISE J111838.70+312537.9 (W1118), WISEA J215018.25-752039.7B (W2150B), and Wolf 1130C. W1118 is a distant companion to a quadruple system composed of F and G stars (Wright et al. 2013). S1416B and W2150B are companions to L dwarfs (Birmingham et al. 2010; Faherty et al. 2020). Wolf 1130C is a companion to an sdM and white dwarf binary (Mace et al. 2013a). W1118, S1416B, and Wolf 1130C are members of metal-poor systems with  $[m/H] = -0.3$ ,  $[m/H] \approx -0.3$ , and  $[m/H] \approx -0.75$ , respectively (Wright et al. 2013; Kesseli et al. 2019; Gonzales et al. 2020).

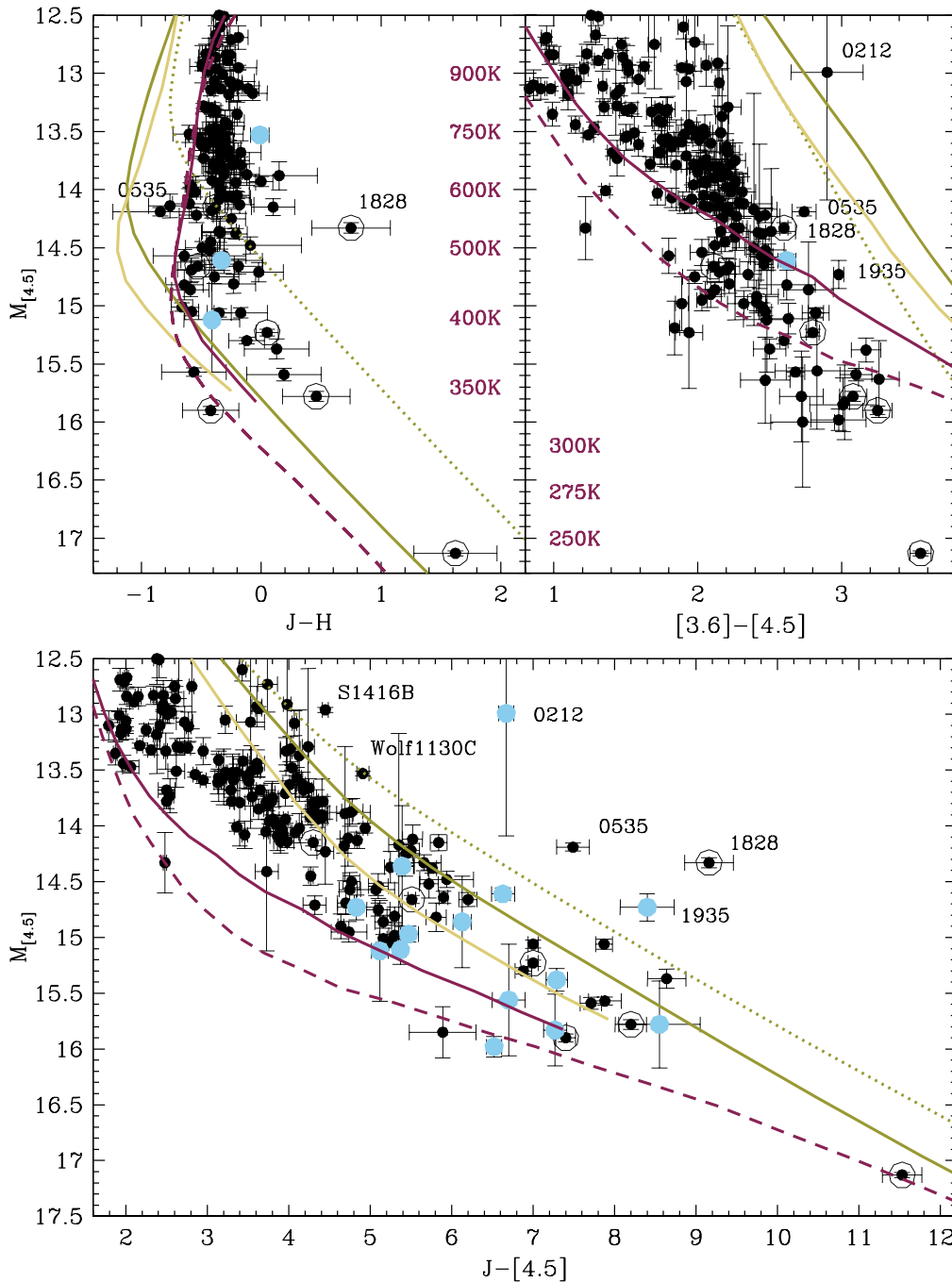
bands brighten when the  $\text{NH}_3$  absorption decreases, and  $[4.5]$  becomes fainter due to increased CO. For a representative 400 K brown dwarf with  $\log g = 4.5$ , the ATMO 2020 models with no mixing and with strong mixing ( $\log K_{zz} = 6$ ) give  $\delta H = -0.7$ ,  $\delta W3 = -0.2$ , and  $\delta [4.5] = +0.3$ .

However, although the nonequilibrium chemistry models reproduce much of the data in Figures 2 and 3, Figure 2 shows

that all models diverge from the observed  $J-K$  and  $[3.6] - [4.5]$  colors for  $T_{\text{eff}} \lesssim 600$  K. Discrepancies between observations and synthetic colors are also apparent in the  $J - [4.5]:M_{[4.5]}$  plot in Figure 3.

Figure 4 shows observed mid-infrared colors for M, L, T, and Y dwarfs which can be used to estimate 5–20  $\mu\text{m}$  colors of cool dwarfs, for example, for JWST observations. If used for





**Figure 3.** Color-magnitude diagrams for late-T and Y dwarfs. Symbols and lines are as in Figure 2. Approximate  $T_{\text{eff}}$  values along the top middle axis are from the ATMO 2020 nonequilibrium chemistry models. Over-luminous Y dwarfs that are possibly unresolved binaries are identified: CWISEP J021243.55+053147.2, WISE J053516.80-750024.9, WISEPA J182831.08+265037.8, and CWISEP J193518.59-154620.3. In the lower panel, the metal-poor T dwarfs S1416B and Wolf 1130C are identified (see also Figure 2).

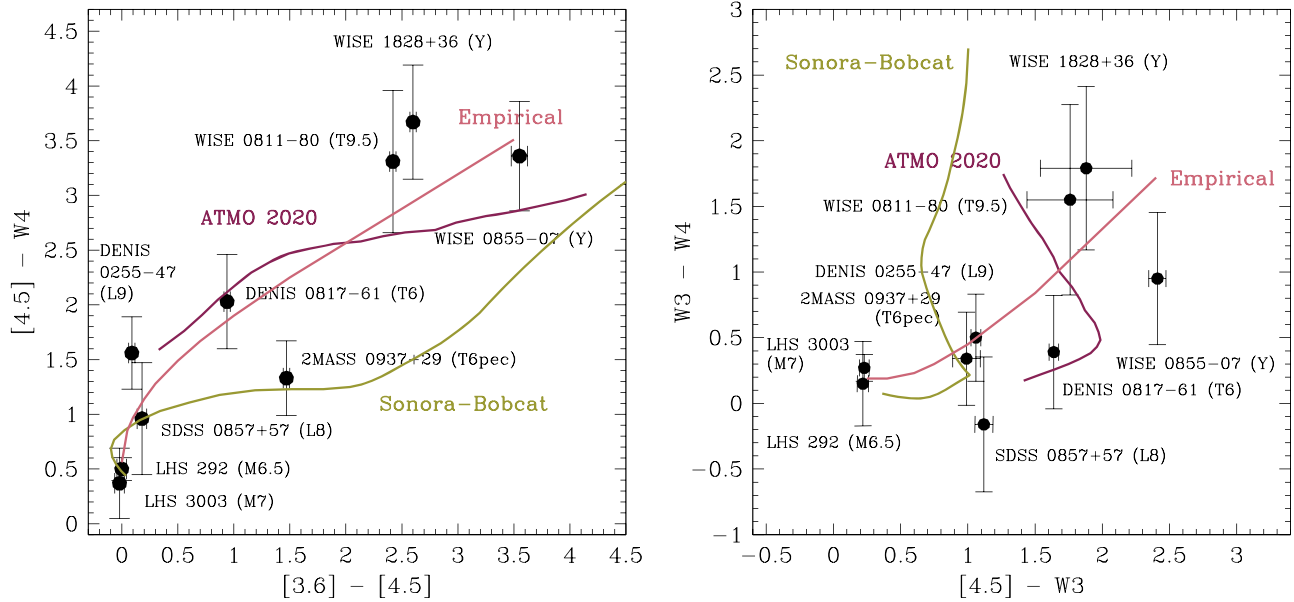
this purpose, the reader should note that the uncertainties are large and exposure estimates should therefore be conservative. We include a by-eye empirical sequence that can be used for interpolation. It is important to note that *chemical equilibrium models will underestimate the  $[4.5] - W3$  and  $[4.5] - W4$  colors of T and Y dwarfs by  $\sim 1$  magnitude.*

#### 4. Modifications to Brown Dwarf Model Atmospheres

Given the discrepancies between observations and models for brown dwarfs with  $T_{\text{eff}} < 600$  K (Figures 2 and 3), we explored modifications to the model structure. We used the

ATMO 2020 models that include strong mixing, as the starting point, as overall they reproduce the observations better than the chemical equilibrium models.

Energy transport in a cool dwarf atmosphere is predominantly convective, with radiative cooling becoming important high in the atmosphere where the pressure is too low for convection to be efficient. Convection is treated as an adiabatic process where pressure  $P$  and temperature  $T$  are defined by  $P^{(1-\gamma)}T^\gamma = \text{constant}$ . For an ideal gas,  $\gamma$  is the ratio of specific heats at constant pressure and volume and, for a gas composed entirely of molecular hydrogen,  $\gamma = 1.4$ . The reader is referred



**Figure 4.** Mid-infrared color-color diagram for M, L, T, and Y dwarfs. Model sequences are cloud-free, with solar metallicity and  $\log g = 4.5$ . Olive green lines are Sonora-Bobcat chemical equilibrium sequences for  $250 \leq T_{\text{eff}} \text{ K} \leq 2400$ , and dark red are ATMO 2020 nonequilibrium chemistry sequences for  $330 \leq T_{\text{eff}} \text{ K} \leq 1280$ . The Sonora-Bobcat chemical equilibrium models reproduce the mid-infrared colors of late-M to late-L-type dwarfs, and the ATMO 2020 nonequilibrium chemistry models reproduce the colors of late-L to late-T dwarfs. An empirical by-eye sequence is shown, which combines the two, and uses the observations of the Y dwarfs to anchor the red end of the sequence.

to Marley & Robinson (2015) and Zhang (2020) for reviews of the important processes in model atmospheres.

One-dimensional models, such as the ATMO and Sonora-Bobcat models, represent the atmosphere as a  $P - T$  profile that maps the cooling from the core out to the surface, and by a chemical abundance profile that maps the chemical changes that occur through the atmosphere as  $P$  and  $T$  change. The  $P - T$  profile can be thought of as a slice through the atmosphere, where both temperature and pressure decrease with increasing altitude.

Of course, an actual brown dwarf atmosphere is more complex. These objects rotate rapidly with periods of a few hours, similar to the solar system giant planets (Zapatero Osorio et al. 2006; Cushing et al. 2016; Espin et al. 2016; Leggett et al. 2016b; Scholz et al. 2018; Vos et al. 2020; Tannock et al. 2021). They also have a radius approximately equal to Jupiter’s (e.g., Burrows et al. 1997). The atmospheres are turbulent, and are likely to have planetary-like features such as zones, spots, and planetary-scale waves (Apai et al. 2017; Showman et al. 2019). Showman & Kaspi (2013) simulate the dynamics of a brown dwarf atmosphere and demonstrate that for a rotation period of a few hours, large-scale, organized horizontal wind speeds of tens of meters per second are plausible, and coherent vertical circulation moves air parcels over a scale height ( $\sim 7 \text{ km}$ ) in  $\sim 10^5 \text{ s}$ . These motions translate into a diffusion parameter  $K_{zz} \sim 10^6 \text{ cm}^2 \text{ s}^{-1}$ , typical of the values used in the ATMO 2020 nonequilibrium chemistry models (Phillips et al. 2020, their Figure 1). The coefficient is higher in the atmospheres of Jupiter and Saturn where  $K_{zz} \approx 10^8 \text{ cm}^2 \text{ s}^{-1}$  (Wang et al. 2016). The  $\lambda \sim 5 \mu\text{m}$  spectrum of the very cold brown dwarf J0855 is also best fit with a high mixing coefficient of  $K_{zz} \approx 10^{8.5} \text{ cm}^2 \text{ s}^{-1}$  (Miles et al. 2020, and Section 5.2).

Augustson & Mathis (2019), and references therein, describe how convection in a rotating stellar or planetary atmosphere can change the chemical composition and thermodynamic

properties of the gas and therefore impact the differential rotation, opacity, and thermodynamic gradients of the atmosphere. The model developed by Augustson & Mathis (2019) connects the rotation rate and vertical diffusion coefficient to the velocity of the gas motion, the divergence from adiabacity, and characteristic scale lengths. The damping effect of rotation can decrease the size of the convection zone, leading to sharper thermodynamic and chemical gradients than would otherwise be present. Furthermore, both superadiabatic and subadiabatic temperature gradients can exist in the atmosphere.

The atmospheres of the solar system giant planets are not perfectly adiabatic (e.g., Guillot et al. 1994; Guillot 2005; Vazan & Helled 2020) and various mechanisms can produce a nonadiabatic cooling curve in giant planet and brown dwarf atmospheres. These include compositional changes such as those due to condensation (e.g., Robinson & Catling 2012), or the  $\text{CO} \rightleftharpoons \text{CH}_4$  changes at the L- to T-type spectral transition (Tremblin et al. 2015, 2019). The upper atmosphere can be heated by a cloud deck, or by breaking gravity waves (e.g., Schubert et al. 2003; O’Donoghue et al. 2016). Further evidence in support of nonadiabatic  $P - T$  profiles in brown dwarf atmospheres comes from retrieval analyses. Line et al. (2015, 2017) and Zalesky et al. (2019) reproduce near-infrared observations of T and Y dwarfs with nonadiabatic  $P - T$  curves, and Piette & Madhusudhan (2020) show that a parametric  $P - T$  profile can be used to determine accurate atmospheric parameters from a high precision spectrum of a T dwarf.

In summary, there is significant evidence that the  $P - T$  curve of a brown dwarf atmosphere does not, and should not be expected to, follow the standard adiabat. In this work we treat the adiabatic parameter  $\gamma$  as a variable, along with  $T_{\text{eff}}$ ,  $g$ ,  $[M/H]$ , and  $K_{zz}$ , and generate a small number of models to compare to observations of a sample of cold brown dwarfs. In the ATMO 2020 models, the initial value of  $\gamma$  is determined for each atmospheric layer using the equation of state tables from

Saumon et al. (1995); for our tuned models we force  $\gamma$  to be constant in the upper atmosphere. The tuning process is described in the next section.

The models are cloud-free, and clouds are not expected to be significant in the photospheres of 400–600 K brown dwarfs (Morley et al. 2012, 2014). However, for the warmest atmospheres in our sample there may be chloride and sulfide clouds in deep regions that can contribute flux at wavelengths where the atmosphere is clear. For the coldest objects, water clouds may form high in the atmosphere, and these would impact the SED at wavelengths where the atmosphere is opaque. We discuss this further in Section 5.3.

The ATMO 2020 models we use here have a fixed potassium abundance. Phillips et al. (2020) show that different treatments of potassium broadening produce large variations in the shape of the blue wing of the  $Y$ -band flux peak in brown dwarfs. Those authors note that an order of magnitude reduction in the  $K$  abundance improves the agreement between models and observations, and suggest that current modeling of the potassium chemistry, including its condensation into  $KCl$ , is slightly incorrect. In this work we adopt a  $K$  abundance of  $4 \times 10^{-9}$  for the late-type  $T$  dwarf we use as a proof of concept, UGPS J072227.51-054031.2 (hereafter J0722). For the cooler  $Y$  dwarfs, we adopt a  $K$  abundance of  $1 \times 10^{-9}$ . We return to the issue of potassium and the  $Y$  band in Section 6.1.

The analysis presented here is a first step toward including processes currently missing in all brown dwarf models. We simplify the complex three-dimensional turbulent atmospheres by parameterizing the  $P$ – $T$  profile in a one-dimensional model. We show below that this simple approach significantly improves the agreement with observations.

## 5. Tuning the Pressure–Temperature Profile

### 5.1. Proof of Concept: The 500 K Brown Dwarf UGPS J0722

We use observations of the bright late-type  $T$  dwarf J0722 for our initial test. This brown dwarf has  $T_{\text{eff}} \approx 500$  K and has extensive observational data, including spectra at  $\lambda \sim 3.5 \mu\text{m}$  and  $\lambda \sim 4.8 \mu\text{m}$  (Lucas et al. 2010; Leggett et al. 2012; Miles et al. 2020). Table 3 lists previous determinations of the atmospheric parameters of J0722. Leggett et al. (2012) compare the observed near-infrared and  $\lambda \sim 3.5 \mu\text{m}$  spectra of J0722, and mid-infrared photometry, to chemical nonequilibrium cloud-free Saumon et al. (2012) models. Constrained by luminosity, they find a range in the  $[T_{\text{eff}}, \log g]$  parameters of  $[492, 3.5]$  to  $[550, 5.0]$ . The mid-infrared observations pushed the parameter selection to the lower temperatures and gravities, while the near-infrared was better fit by the higher temperature and gravity solution. Filippazzo et al. (2015) and Dupuy & Kraus (2013) also use luminosity-based arguments to determine the parameters given in Table 3, while Miles et al. (2020) use the Sonora-Bobcat model grid and near- and mid-infrared photometry to constrain  $T_{\text{eff}}$ , evolutionary models to constrain  $g$ , and the  $4.8 \mu\text{m}$  spectrum to constrain  $K_{\text{zz}}$ .

The top panel of Figure 5 shows SEDs generated by standard models with parameters typical of those found for J0722. As found in earlier analyses (e.g., Leggett et al. 2012; Miles et al. 2020), the fit is quite good, especially for the nonequilibrium chemistry models. However the calculated  $YJ$  fluxes are higher than observed and the  $2 \lesssim \lambda \mu\text{m} \lesssim 4$  flux is lower than observed. The direction of these offsets is consistent with the

systematic discrepancies seen in the colors of the cooler brown dwarfs in Figures 2 and 3:

1. The modeled  $J - H$  and  $J - [4.5]$  are too blue because  $J$  (in particular, see Figure 5) is too bright,
2. The modeled  $J - K$  is much too blue because  $J$  is too bright and  $K$  too faint,
3. and the modeled  $[3.6] - [4.5]$  is too red because  $[3.6]$  is too faint.

In other words, the discrepancies demonstrated in the top panel of Figure 5, for standard models, apply to all brown dwarfs with  $T_{\text{eff}} < 600$  K.

Panel (b) of Figure 5 shows a model we have tuned to better fit the observations. The tuning is done manually, iterating over ages of 100 Myr, 1 Gyr, 5 Gyr, and 10 Gyr, and metallicities of  $-0.5$ ,  $0$ , and  $+0.3$  dex. The steps involved are:

1. Assume a priori that  $\log K_{\text{zz}} = 7$
2. Select  $\log g$  and radius based on evolutionary models for the selected age
3. Select  $T_{\text{eff}}$  to reproduce the observed flux at  $[4.5]$
4. Decrease  $\gamma$  to reduce the  $YJHK$  flux
5. Let  $\gamma$  increase to the standard value at a depth in the atmosphere defined by pressure  $P(\gamma, \text{max})$ , and deeper, to increase the  $YJ$  flux as necessary
6. Adjust  $\log K_{\text{zz}}$  if the other adjustments have changed the  $[4.5]$  flux.

The fits are also constrained by ensuring that the scaling used to transform the model surface flux to that detected at Earth, which depends on the distance to the dwarf and its radius, is consistent with the evolutionary models. Once a reasonable fit is obtained, judged by eye for this preliminary analysis, selection between any similar quality fits is done by choosing the fit that best agrees with the observed  $[3.6]$  and  $W3$  photometry.

Figure 6 illustrates the sensitivity of the synthetic  $0.9$ – $20 \mu\text{m}$  spectrum to the parameters (for these models, longer wavelengths of  $20$ – $30 \mu\text{m}$  do not show significant sensitivity). The shape of the SED is very sensitive to temperature, and also to metallicity.  $\gamma$  impacts the slope from the near- to the mid-infrared, as well as the depth of the strong absorption bands. Gravity signatures are more subtle, and somewhat degenerate with metallicity. However gravity is also constrained by the flux scaling to Earth, via the mass–radius relationship used by the evolutionary models. We discuss this further in Section 5.5.

The SED generated by the tuned model provides a significantly improved fit to observations of J0722. The agreement with the near-infrared spectrum and the  $4 \leq \lambda \mu\text{m} \leq 5$  spectrum is now excellent, instead of being a factor of  $\sim 3$  discrepant. Also, the discrepancy at the bottom of the strong  $3.3 \mu\text{m}$   $\text{CH}_4$  band is reduced to a factor of  $\sim 2$  from a factor of  $\sim 10$ . Apart from the reduced adiabat, the other atmospheric parameters— $T_{\text{eff}}$ ,  $g$ ,  $[m/H]$  and  $K_{\text{zz}}$ —are consistent with previous determinations (Table 3). Panel (d) of Figure 5 compares the spectra generated for J0722 by the standard and tuned nonequilibrium chemistry ATMO 2020 models. The difference in the near-infrared region is clear, as is that in the  $2$ – $4 \mu\text{m}$  region. JWST spectra at  $5$ – $9 \mu\text{m}$ , impossible to obtain from the ground, will provide an additional check on this approach.

Figure 7, top right panel, shows the standard and tuned  $P$ – $T$  diagram for J0722, as well as the contribution function—

**Table 3**  
Atmospheric Parameters for the  $P - T$  Tuned Brown Dwarf Sample

Name	$V_{\tan}$ $\text{km s}^{-1}$	Previous Work					This Work						Evol. Model	
		$T_{\text{eff}}$ K	$\log g$ $\text{cm s}^{-2}$	[m/H]	$\log K_{\text{zz}}$ $\text{cm}^2 \text{s}^{-1}$	Ref.	$T_{\text{eff}}$ K	$\log g$ $\text{cm s}^{-2}$	[m/H]	$\log K_{\text{zz}}$ $\text{cm}^2 \text{s}^{-1}$	$\gamma$	$\Delta\gamma(\text{P}, \text{T})$ bar, K	$\sim \text{Mass}$ $M_{\text{Jup}}$	$\sim \text{Age}$ Gyr
WISEA J035000.31 −565830.5	16.8 $\pm 0.3$	310–340 300–350 294–341	3.75–4.25 $\sim 5.00$ 3.92–4.47	$\gg 0$	6.0	Le17 Sc15 Du13 <sup>a</sup>	325	4.0	+0.3	6.0	1.30	(15,860)	5	1.0
UGPS J072227.51 −054031.2	18.9 $\pm 0.2$	522–558 524–614 493–551 490–520	3.70–4.40 4.15–5.21 4.38–4.92 3.50–4.50	$\sim 0$ $\sim 0$	4.4 5.5	Mi20 Fi15 Du13 <sup>a</sup> Le12	540	4.50	0.0	7.0	1.27	...	15	1.5
WISE J085510.83 −071442.5	88.0 $\pm 0.6$	249–260 240–260 $\sim 240$	3.50–4.50 3.50–4.30 $\sim 4.00$		8.5 6.0	Mi20 Le17 Lu16	260	4.00	0.0	8.7	1.33	(50,870)	5	3.0
WISEPA J154151.66 −225025.2	25.7 $\pm 0.4$	396–434 302–474 360–390 $\approx 400$ 335–367	4.30–4.90 3.72–4.24 4.25–4.75 4.00–4.50 4.03–4.54	$> 0$	6.0 6.0	Mi20 Za19 Le17 Sc15 Du13 <sup>a</sup>	375	4.50	+0.3	6.0	1.27	(12,760)	12	3.0
WISEPA J182831.08 +265037.8AB <sup>b c</sup>	48.6 $\pm 1.1$	310–340 421–470	3.75–4.25 4.24–4.78	$\ll 0$	6.0	Le17 Du13 <sup>a</sup>	375	4.0	−0.5	7.0	1.20	(7,640)	5	0.5
WISEPC J205628.90 +145953.3	33.6 $\pm 0.5$	471–522 447–523 410–440 400–450 414–460	4.40–5.00 4.64–5.18 4.25–4.75 4.00–4.50 4.23–4.76	$> 0$	5.3 6.0	Mi20 Za19 Le17 Sc15 Du13 <sup>a</sup>	475	4.25	0.0	7.0	1.20	(7.5,820)	8	0.5
WISEA J220905.75 +271143.6	53.2 $\pm 0.8$	310–340 500–550	4.27–4.75 4.00–4.50	$> 0$	6.0	Le17 Sc15 <sup>d</sup>	350	4.00	0.0	7.0	1.25	(10,740)	5	0.5

**Notes.** Excluding any systematic errors, we estimate the uncertainties in our derived parameters to be  $\pm 20$  K in  $T_{\text{eff}}$ ,  $\pm 0.25$  dex in  $\log g$ ,  $\pm 0.3$  dex in [m/H],  $\pm 1$  dex in  $\log K_{\text{zz}}$ ,  $\pm 0.1$  in  $\gamma$ , and  $\pm 10$  bar in  $P_{\gamma-\text{max}}$  (Figure 6). These uncertainties lead to an uncertainty in mass and age of a factor of  $\sim 2$  and  $\sim 3$ , respectively (Section 5.5).

<sup>a</sup> The Dupuy & Kraus (2013)  $T_{\text{eff}}$  and  $\log g$  values quoted in the table use the bolometric luminosities given in that paper combined with the more recent measurements of parallaxes used here.

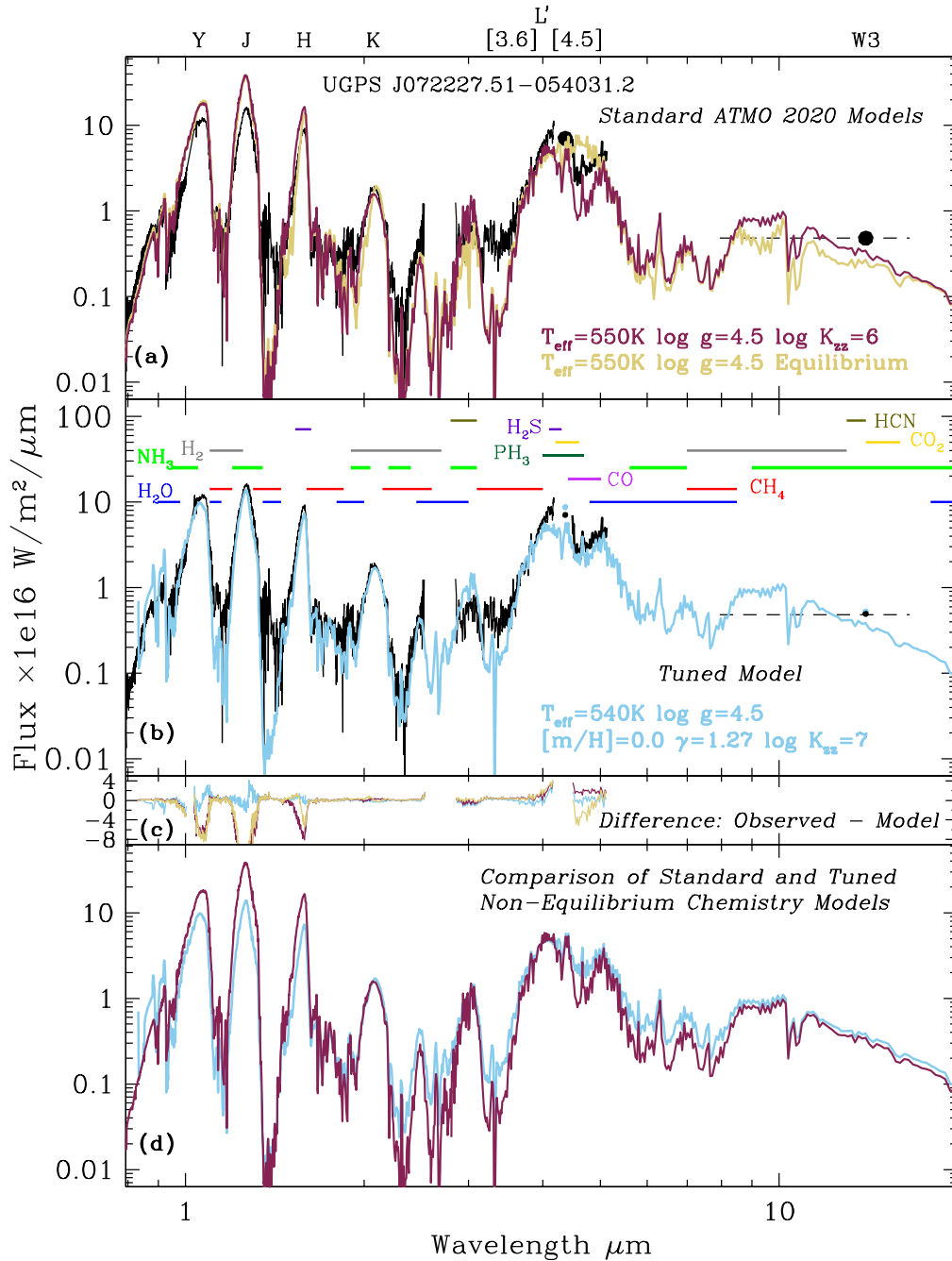
<sup>b</sup> J1828 could not be fit by us as a single star. The parameters given here and the fits shown in Figure 8 assume it is an equal-mass binary system.

<sup>c</sup> The Dupuy & Kraus (2013) higher temperature for J1828 is based on the assumption that it is a single object.

<sup>d</sup> A value as high as 500 K for  $T_{\text{eff}}$  is not plausible for J2209, as also pointed out by Martin et al. (2018). We suspect the noisy near-infrared spectrum skewed the model fit by Schneider et al. (2015).

**References.** Du13—Dupuy & Kraus (2013), Fi15—Filippazzo et al. (2015), Le12—Leggett et al. (2012), Le17—Leggett et al. (2017), Lu16—Luhman & Esplin (2016), Mi20—Miles et al. (2020), Sc15—Schneider et al. (2015), Za19—Zalesky et al. (2019, constrained). Tangential velocities are from Kirkpatrick et al. (2019).



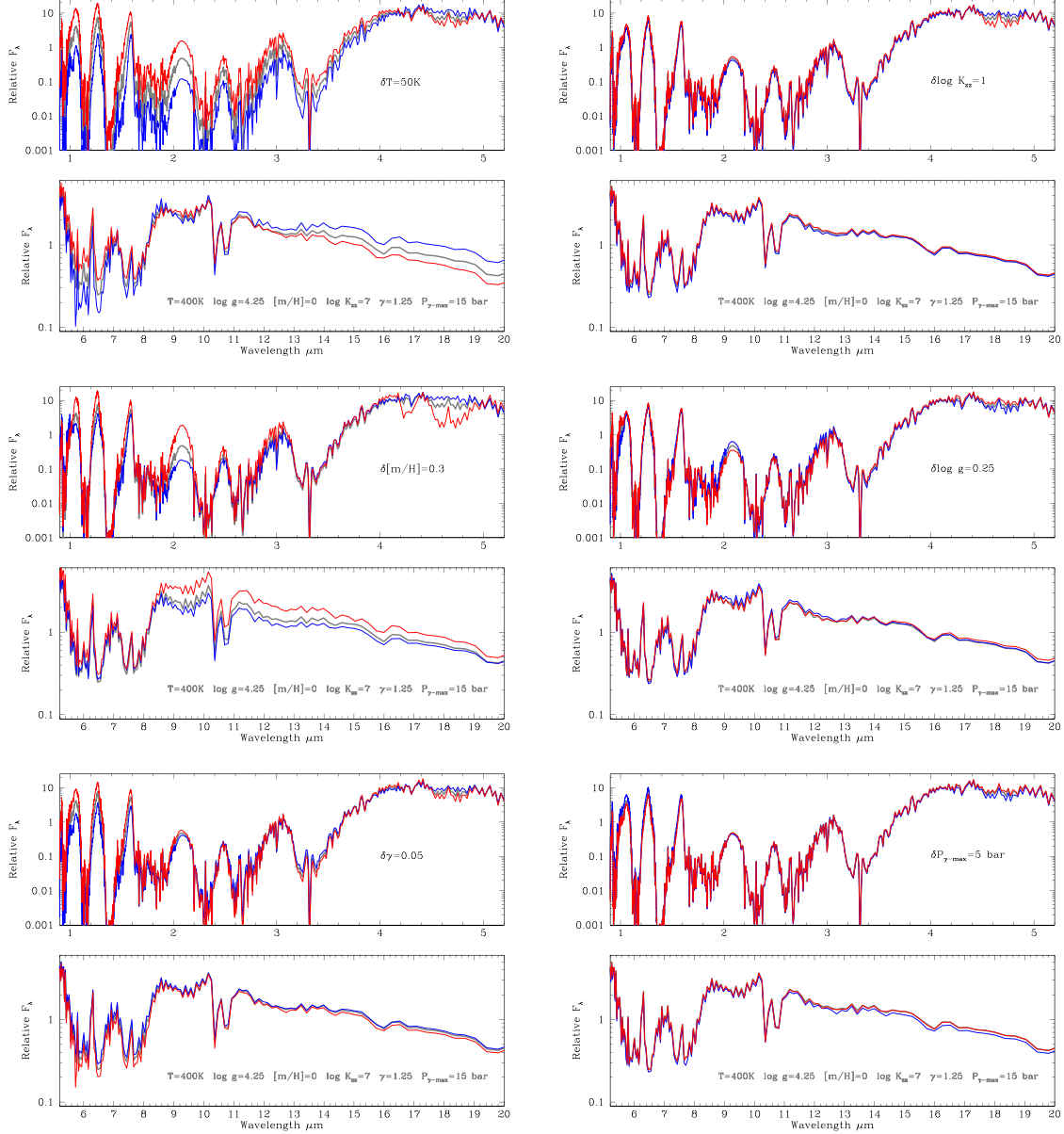


**Figure 5.** The black line is the flux-calibrated spectrum of UGPS J072227.51–054031.2 (Lucas et al. 2010; Leggett et al. 2012; Miles et al. 2020). The black circles are the observed Spitzer [4.5] and WISE W3 photometric data points, and the dashed line indicates the width of the W3 filter which peaks at  $\lambda \sim 14 \mu\text{m}$ . The colored lines are ATMO 2020 models with parameters given in the legends. Significant absorbers are identified at the top of panel (b). Also in panel (b), the small blue and black data points demonstrate the good agreement between the observed and tuned model photometry in the mid-infrared. Panel (c) demonstrates the improvement in fit provided by the tuned model (note the linear y-axis). Panel (d) compares the standard and tuned ATMO 2020 nonequilibrium models. Note that the model fluxes are not scaled to match the data, they are scaled by the measured distance and by the brown dwarf radius calculated by ATMO 2020 evolutionary models. The observed and tuned model data as shown in panel (b), is available in machine-readable format as the data behind the Figure.

(The data used to create this figure are available.)

the pressure or atmospheric layer from which flux at a certain wavelength arises. Standard curves for a  $T_{\text{eff}}$  value equal to that determined from the fit, and a temperature 100 K cooler, are shown; these demonstrate that the tuned model has an interior (where the  $\lambda \sim 1 \mu\text{m}$  flux originates) similar to the cooler

standard model, and an upper atmosphere similar to the warmer standard model. The fact that the  $3.3 \mu\text{m}$  feature is still somewhat deeper than observed suggests that the revised  $P - T$  profile may not be warm enough where this flux originates, in the upper atmosphere at pressures  $\sim 0.1$  bar. Interestingly, the



**Figure 6.** Comparison of the effects of varying the model parameters in our tuning process, for a representative  $T_{\text{eff}} = 400$  K model. Each variation of the six parameters is displayed as a plot pair, with the near-infrared region in the upper plot and the mid-infrared in the lower. The gray line shows the SED for the model with parameters as in the legend. Red and blue lines show the SEDs generated by increasing or decreasing the parameter, respectively. The parameter that is being varied is shown in the upper panel. The spectra are normalized to a value of 10 at  $\lambda = 4.98 \mu\text{m}$  (a local flux maximum).

need for upper-atmosphere heating has also been identified in retrieval analyses of L dwarf atmospheres (Burningham et al. 2017). We discuss this further in Section 6.

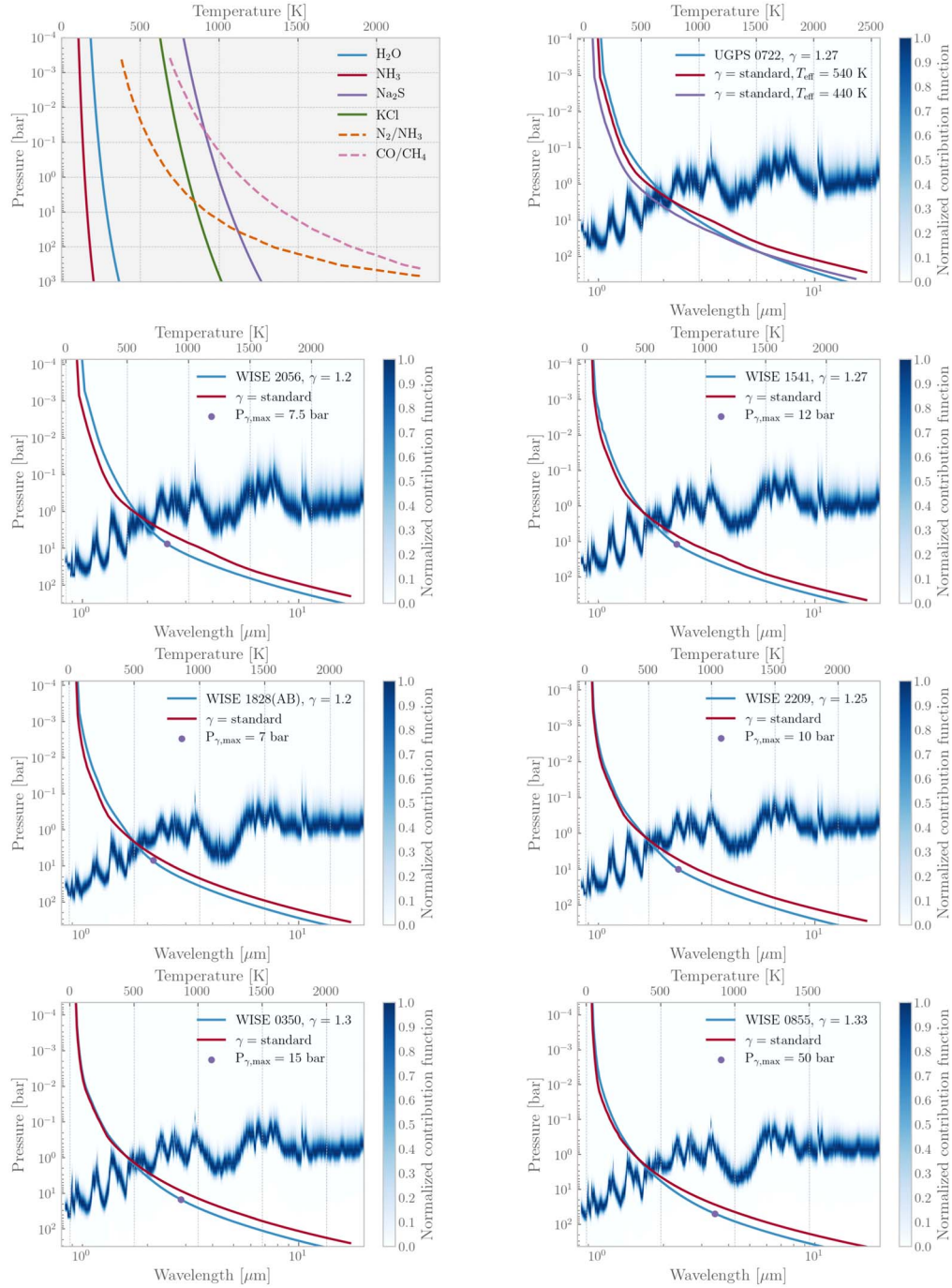
### 5.2. Tuned-model Fits to 250–500 K Brown Dwarfs

We extended the approach described above to colder brown dwarfs. The sample consists of three cold brown dwarfs for which Miles et al. (2020) provide  $\lambda \approx 4.8 \mu\text{m}$  spectra, because this region is sensitive to mixing of  $\text{CH}_4$  and CO (Figures 5 and 6): J0855, WISEPA J154151.66–225025.2 (hereafter J1541), and WISEPC J205628.90+145953.3 (hereafter J2056). We added three other brown dwarfs with  $J - [4.5]$  colors between those of J2056 and J1541, and the extreme dwarf J0855, all of

which have W3 photometry available—WISE J035000.31–565830.5 (hereafter J0350), WISEPA J182831.08+265037.8 (hereafter J1828), and WISE J220905.73+271143.9 (hereafter J2209).

Figures 2 and 3 identify the target objects in the color–color diagrams, and Table 3 lists the six objects, with atmospheric parameters determined here and previously. We could not fit the absolute flux level of J1828 as a single object, but we did find a satisfactory fit assuming it is an equal-mass binary. We refer to J1828 from here on as J1828(AB) to clarify that the estimated properties assume binarity.

Figures 8 and 9 show the SEDs of the six Y dwarfs in our sample—observational data as well as the best by-eye tuned model spectrum—in order of decreasing  $T_{\text{eff}}$ . The W4



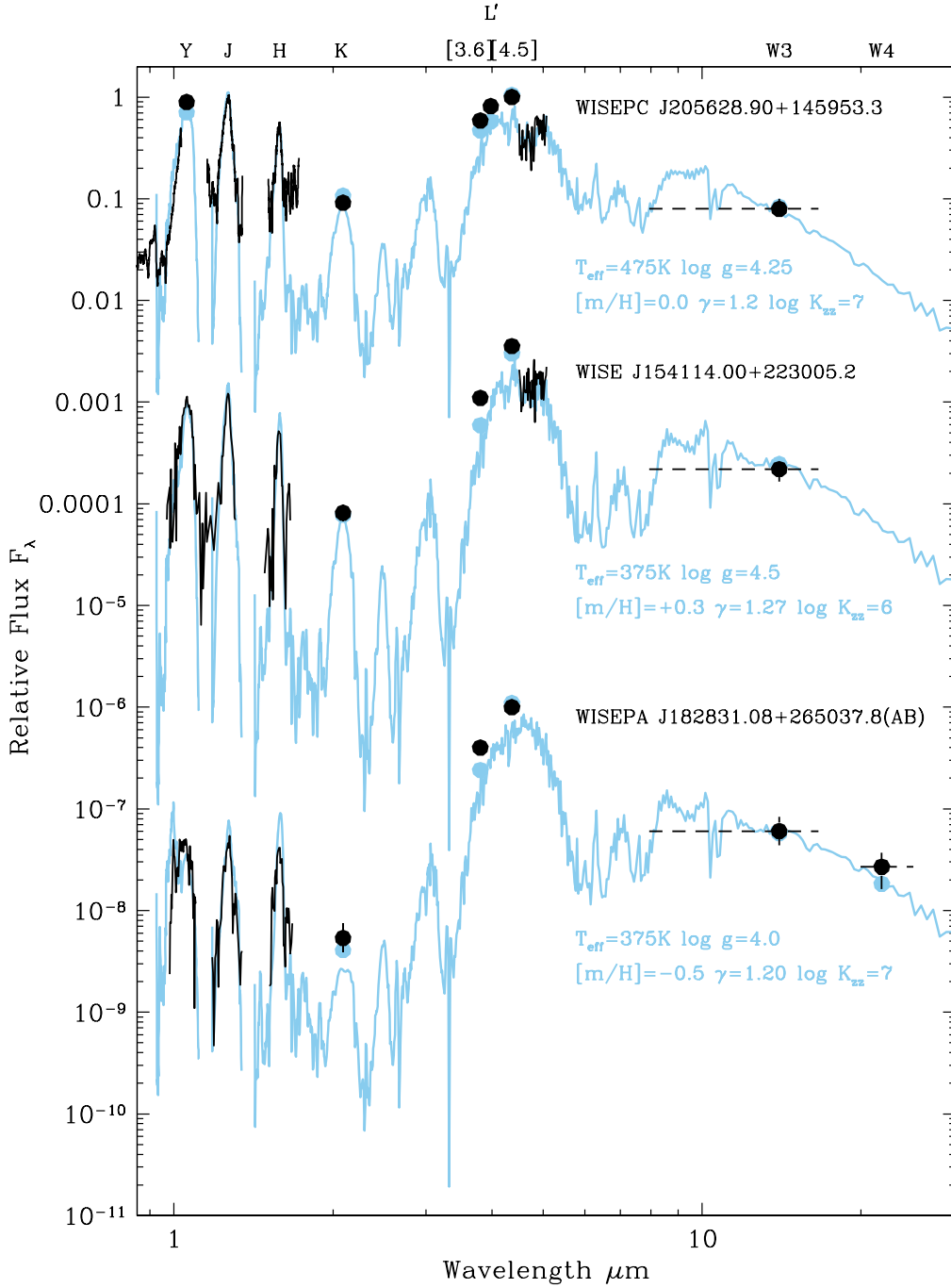
**Figure 7.** The top left panel shows condensation curves for elements in equilibrium (see the text for discussion). The other panels are pressure–temperature profiles (left and upper axes) and flux contribution functions (thick blue line, left and lower axes), for the brown dwarfs in our tuning sample. Blue  $P - T$  profiles are tuned to fit the data by reducing the adiabat  $\gamma$  at  $P < P_{\gamma,\text{max}}$ ; red lines have a standard radiative-convective profile.

photometric point is included for J1828(AB) and J0855 in the Figures; it was not used when judging fit quality as the uncertainty is large (Table 2), but the observed and modeled photometry agree within the uncertainties.

Note the increasing dominance of the mid-infrared region and the steady reddening of the [3.6] – [4.5] color with decreasing temperature in Figures 8 and 9. Note also the pronounced difference between J1541 and J1828(AB) in Figure 8 although they have the same  $T_{\text{eff}}$ —the lower metallicity and  $\gamma$  of J1828(AB) suppress the  $YJHK$  flux and

broaden the  $Y$  band peak. These changes in the SEDs are also demonstrated in Figure 6. As  $T_{\text{eff}}$  drops to 260 K there is a loss of flux at  $\lambda \sim 1 \mu\text{m}$ .

The fits shown in Figures 8 and 9 are generally very good across the entire SED. The height and width of the near-infrared flux peaks are well reproduced, with the exception of J1828(AB) where the  $H$ -band peak is a factor of  $\sim 2$  too bright, and the  $Y$ -band peak for J0350, where the model is a factor of 3 too faint. The  $Y$ -band discrepancy suggests that a large amount of flux at  $\lambda \lesssim 1.0 \mu\text{m}$  is missing from the models, as the red



**Figure 8.** Adiabatic-tuned fits for three  $T_{\text{eff}} \sim 400$  K brown dwarfs, identified in the legends. Solid black lines are observed spectra (Cushing et al. 2011; Leggett et al. 2013; Schneider et al. 2015; Miles et al. 2020; Cushing et al. 2021), and the black points are observed photometric data, with vertical error bars where these are larger than the symbol. Uncertainties in the observed J2056 spectra are negligible, in the J1541 and J1828(AB) spectra they are 10%–20% in regions where there is significant flux. Dashed black lines indicate the passbands of the broad W3 and W4 filters. Blue lines are synthetic spectra generated by the tuned models with parameters given in the legends, and blue points are the synthetic photometry. The observed and tuned model data is available in machine-readable format as the data behind the Figure.

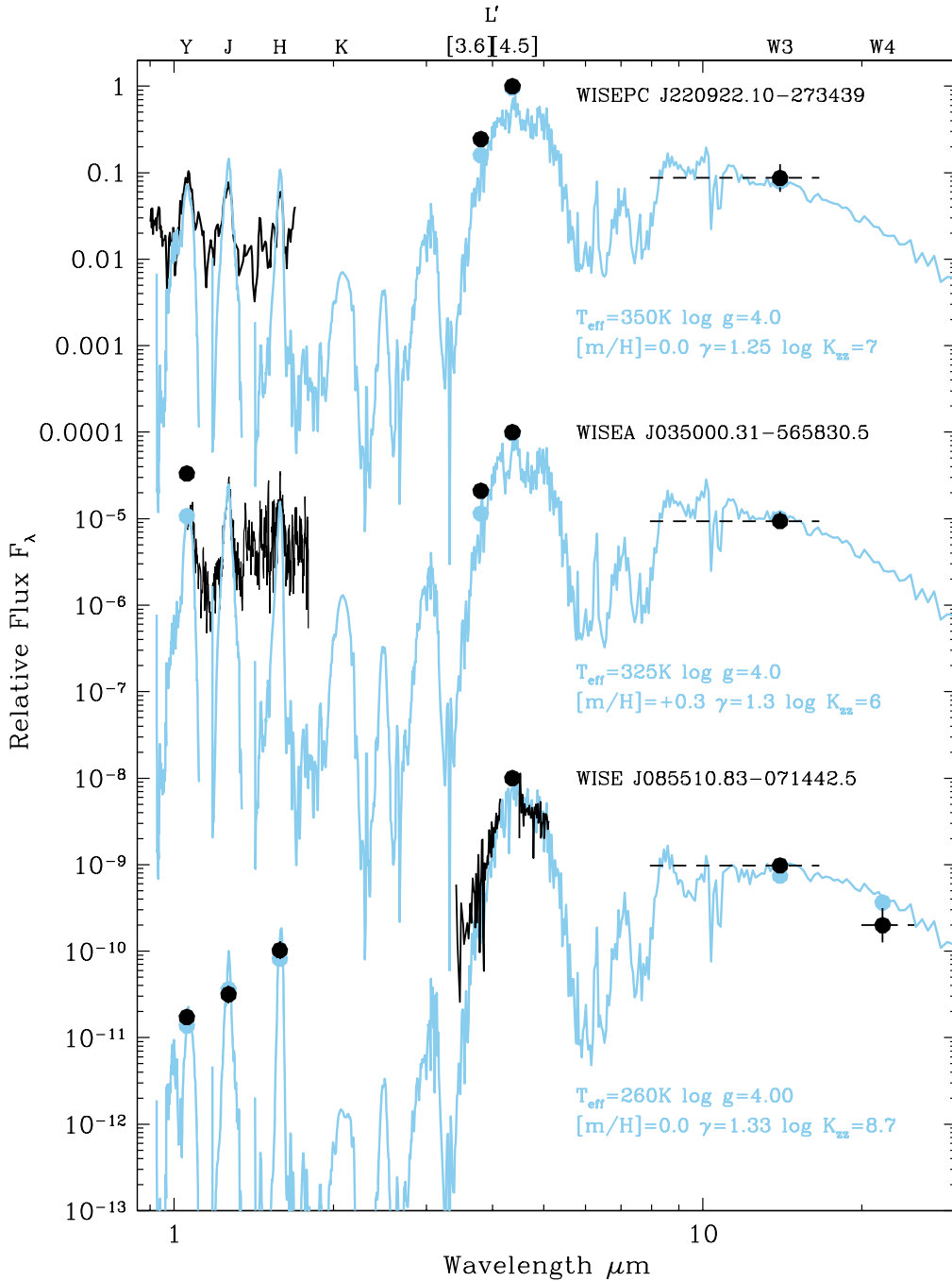
(The data used to create this figure are available.)

wing of the flux peak is well matched. Both these systems are challenging—J1828(AB) is a very metal-poor likely-multiple system, and J0350 is a cold metal-rich brown dwarf.

The model flux at  $\lambda \approx 3.3 \mu\text{m}$  is low, as also seen for J0722 in Figure 5 (although the agreement is improved by a factor of  $\sim 5$  compared to standard-adiabatic models). This leads to [3.6]

magnitudes that are a few-tenths to a magnitude fainter than observed. The spectrum of J0855 in Figure 9 suggests that the loss occurs only at the blue end of the  $3.13 \lesssim \lambda \mu\text{m} \lesssim 3.92$  [3.6] filter bandpass. The mid-infrared fluxes are otherwise well matched. The coldest object, J0855, is very well matched—the observed and synthetic photometry generated by the tuned





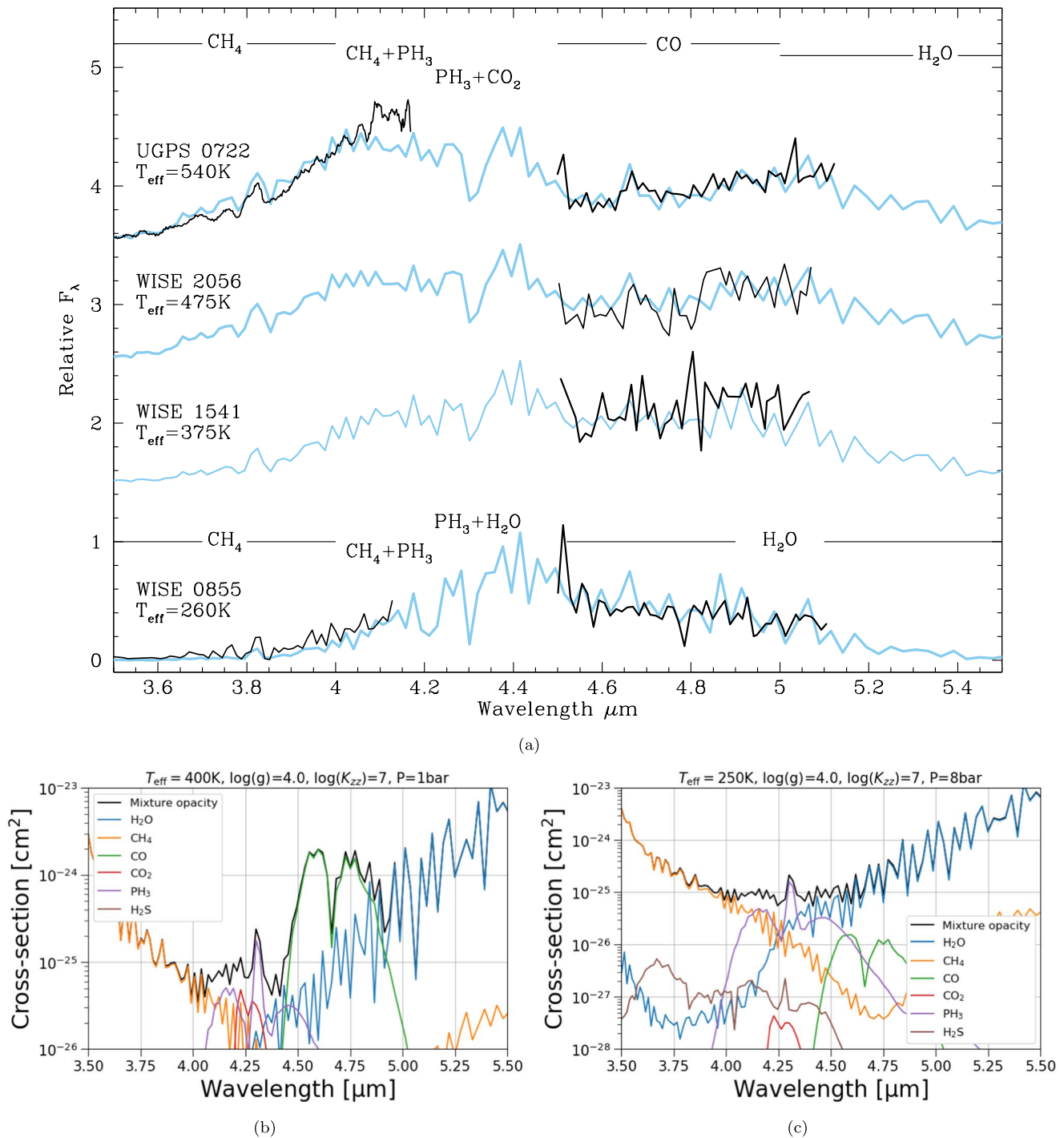
**Figure 9.** Adiabatic-tuned fits for three  $T_{\text{eff}} \sim 300$  K brown dwarfs, identified in the legends. Solid black lines are observed spectra (Schneider et al. 2015; Leggett et al. 2016a; Morley et al. 2018; Miles et al. 2020), and the black points are observed photometric data, with vertical error bars where these are larger than the symbol. Uncertainties in the observed near-infrared spectra, in regions where there is significant flux, are 20%–50% for J2209 and J0350. Uncertainties in the observed spectra for J0855 are 10%–30% for the  $L$  band and 5%–20% for the  $M$  band. The observed and tuned model data is available in machine-readable format as the data behind the Figure.

(The data used to create this figure are available.)

model agree within the measurement uncertainties at all passbands apart from [3.6], and the 3.5–4.1  $\mu\text{m}$  and 4.5–5.1  $\mu\text{m}$  spectra are well reproduced (see also Section 5.4).

The agreement between these tuned nonequilibrium chemistry models and observations is better than has been possible in the past. Previous efforts to fit the mid-infrared spectroscopy and photometry of WISE 0855 by Morley et al. (2018) found

that models with lower  $\text{CH}_4$  abundances could adequately fit the data, including models with subsolar metallicity and C/O ratios (see the low-metallicity sequence in the [3.6] – [4.5] panel in Figure 2). Low-metallicity models that adequately match the mid-infrared photometry are too bright at near-infrared wavelengths, but a deep continuum opacity source (e.g., clouds) could readily decrease the near-infrared flux to match the observed photometry. Those authors found that

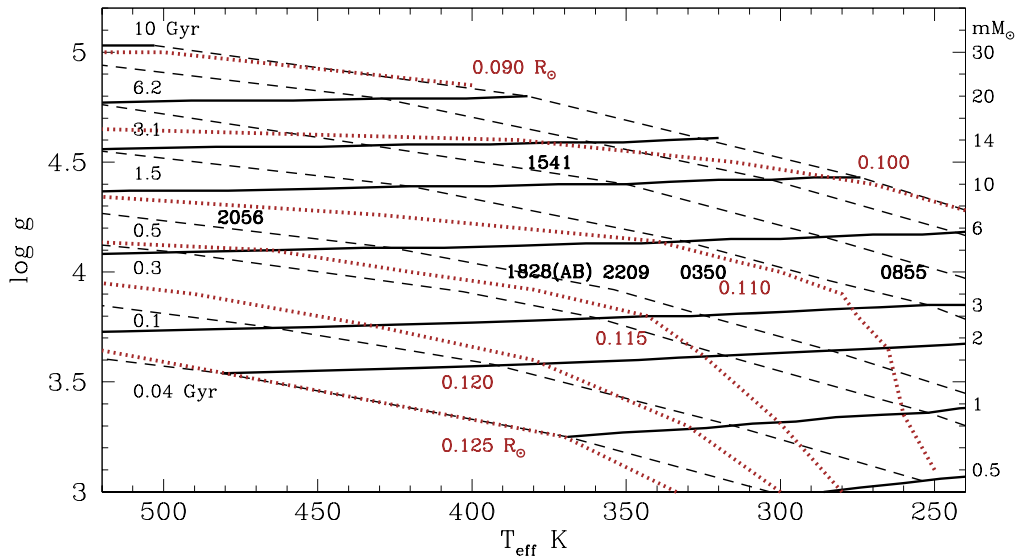


**Figure 10.** The upper panel (a) shows observations (black line) and the tuned-adiabat model spectra (blue line) from Figures 8 and 9, for  $3.5 \leq \lambda \mu\text{m} \leq 5.5$ . The lower panels (b) and (c) show ATMO 2020 opacity calculations for these wavelengths, for two representative values of  $T_{\text{eff}}$ .

upper-atmosphere heating could not be invoked to fit the observed properties, but did not explore changes to the deep adiabatic structure. In other recent work, the model comparisons to J0722, J2056, J1541, and J0855 by Miles et al. (2020, their Figure 3) show large discrepancies (factors of 2–3) at most wavelengths.

Table 3 gives our derived model parameters and compares these to previously determined values. Excluding any systematic errors, we estimate the uncertainties in our derived atmospheric parameters, based on the full fit to the SED, to be  $\pm 20\text{ K}$  in  $T_{\text{eff}}$ ,  $\pm 0.25$  dex in  $\log g$ ,  $\pm 0.3$  dex in  $[\text{m}/\text{H}]$ ,

$\pm 1$  dex in  $\log K_{zz}$ ,  $\pm 0.1$  in  $\gamma$ , and  $\pm 10$  bar in  $P_{\gamma \text{ max}}$ . This is based on the sensitivity of the SED to the parameters (Figure 6); gravity is constrained by both the SED and the mass–radius relationship of the ATMO 2020 evolutionary models (Phillips et al. 2020). The absolute uncertainty in the parameter estimates is difficult to assess but is unlikely to be more than twice these values, given the agreement between the estimates for individual objects in Table 3, which were arrived at using different models and different methods. Furthermore, the ATMO 2020 evolutionary models have been tested against a small sample of brown dwarfs with



**Figure 11.** Evolutionary curves from ATMO 2020 models (<http://opendata.erc-atmo.eu>). Solid black lines are isomass sequences for objects with mass shown along the right axis. Evolution proceeds from left to right. Dashed lines are isochrones for the ages indicated, and dotted brown lines are lines of constant radii, for the values indicated. The location of the six Y dwarfs in our tuning sample are shown by the short name.

dynamically determined masses, and the ages derived are appropriate for the solar neighborhood (Dupuy & Liu 2017; Buder et al. 2019). The evolutionary models also produce cooling curves very similar to earlier models, while using a more recent equation of state for H-He mixtures (Chabrier et al. 2019).

The atmospheric parameters determined for J1541 and J2056 by Zalesky et al. (2019) in Table 3 are of particular relevance, as those authors use a retrieval method to adjust the atmosphere properties in order to reproduce observations, somewhat similar to (but more complex than) our  $P-T$  tuning technique (see Line et al. 2015). Zalesky et al. (2019) constrain their fits using HST near-infrared spectra while we use longer-baseline observations, which allows us to probe the higher and cooler regions of the atmosphere (compare our Figure 7 to Zalesky et al. Figure 2). The shape of the profile we determine for J2056 is similar to that found by Zalesky et al. (2019), with the atmosphere cooler at deeper layers and warmer in the upper layers compared to the grid models. However the difference between the tuned and standard temperatures are larger at deeper layers in our models; for example, at 100 bar we find  $\delta T \approx 500$  K compared to 100 K for Zalesky et al. (2019). For J1541, the deviation of the shape of the profile from the standard model is larger in the Zalesky et al. analysis than in our analysis. Zalesky et al. (2019) find that both the upper and lower regions of the atmosphere are warmer by  $\sim 500$  K, while we find that the deeper layers are cooler with only small differences from standard in the upper regions. Nevertheless both analyses indicate that the  $P-T$  profile deviates from the standard form, typically with cooler regions in the deeper layers of late-T and Y dwarf atmospheres, from which the near-infrared radiation emerges.

The parameters determined by Miles et al. (2020) are also of interest, as the  $4.8 \mu\text{m}$  spectra presented by those authors provides a constraint on  $K_{zz}$ . Both this work and Miles et al. find a very high  $K_{zz}$  for the extremely cold J0855. We are in agreement for J1541; however, Miles et al. find a lower value than ours for J0722 and J2056 (Table 3). We suggest that our estimates are more robust as they are based on broader wavelength coverage.

Our tuning sample of six Y dwarfs has a relatively small range in the photospheric adiabatic parameter  $\gamma$  (typically

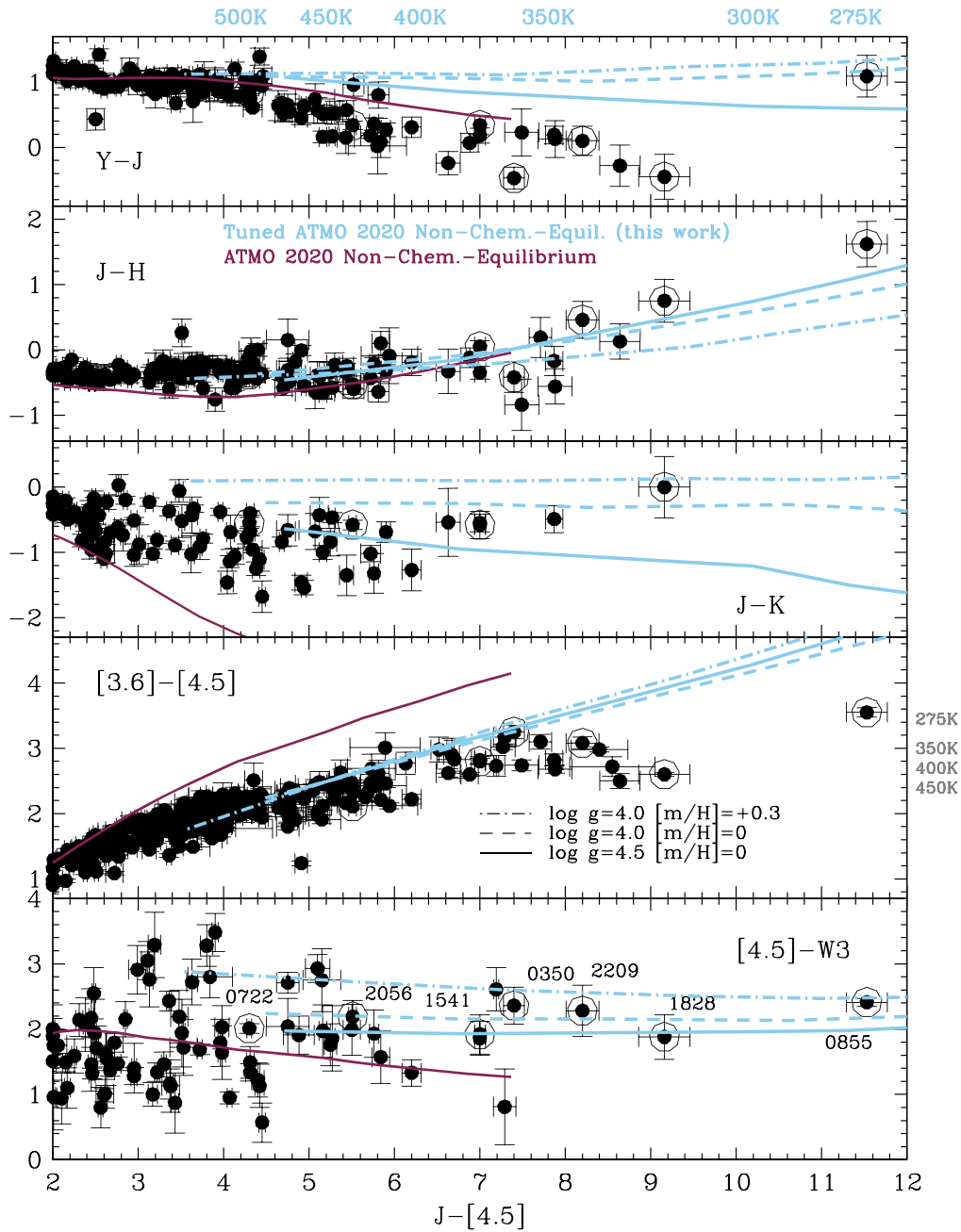
1.2–1.3), and in the diffusion coefficient  $\log K_{zz}$  (typically 6–7), but some variation in these values for a larger sample would not be surprising. The global properties of a brown dwarf atmosphere are likely to vary with inclination to the line of sight. For example, models of turbulent convection in rapidly rotating atmospheres, including the solar system gas giants, calculate that  $K_{zz}$  is latitude dependent, decreasing from the equator to the poles (e.g., Flasar & Gierasch 1978; Visscher et al. 2010; Wang et al. 2016). Measurements of variability are also likely to be inclination dependent (Vos et al. 2017).

### 5.3. Clouds, Chemical Changes, and the Disruption of Convection in Y Dwarfs

Figure 7 shows the standard and modified  $P-T$  profile for the six Y dwarfs in our sample. Also shown is the contribution function, which indicates the pressure layer from which the near- to mid-infrared flux emerges in the tuned model. From the coldest to the warmest object, the  $1 \mu\text{m}$  light emerges from regions where  $P \sim 10$ –100 bar and temperatures are 900–1500 K, while the  $10 \mu\text{m}$  light emerges from regions where  $P \sim 1$  bar and temperatures are 250–500 K. Where the atmosphere is more opaque, such as at  $\lambda \sim 3, 6$ , or  $8 \mu\text{m}$ , the light emerges from high and cold regions where  $P \sim 0.1$  bar and  $T \sim 150$ –350 K.

The condensation curves in the top left panel of Figure 7 suggest that water clouds would be expected in the upper layers of the atmosphere of J0855, and possibly in the very upper atmosphere of J0350 and J2209 (see also Morley et al. 2014, their Figure 6). These could produce the heating in the upper atmosphere needed to increase the model flux at  $\lambda \approx 3.3 \mu\text{m}$ , although this could also be accomplished by breaking gravity waves as is likely in the solar system giant planet atmospheres above the 1 bar pressure surface (e.g., Schubert et al. 2003; O’Donoghue et al. 2016).

The condensation curves also indicate that KCl and  $\text{Na}_2\text{S}$  clouds would be important in the regions where the near-infrared flux originates, for our sample, i.e.,  $P \sim 10$  bar and  $T \sim 1000$  K (see also Morley et al. 2012, their Figure 4). The 10 bar/1000 K level also corresponds to where nitrogen moves



**Figure 12.** Color-color diagrams for late-T and Y dwarfs. Symbols and lines are as in Figure 2, with the addition of modified-adiabat model sequences shown in blue. The model has  $K_{zz} = 10^7$  and  $\gamma = 1.25$  at pressures of 15 bar and lower. Values of  $T_{\text{eff}}$  from this model are shown along the top axis. For the frequently used  $[3.6] - [4.5]$  color diagnostic, the model deviates from observations for the coldest objects, and semiempirical values of  $T_{\text{eff}}$  are shown in gray along the right axis (see Section 6.2).

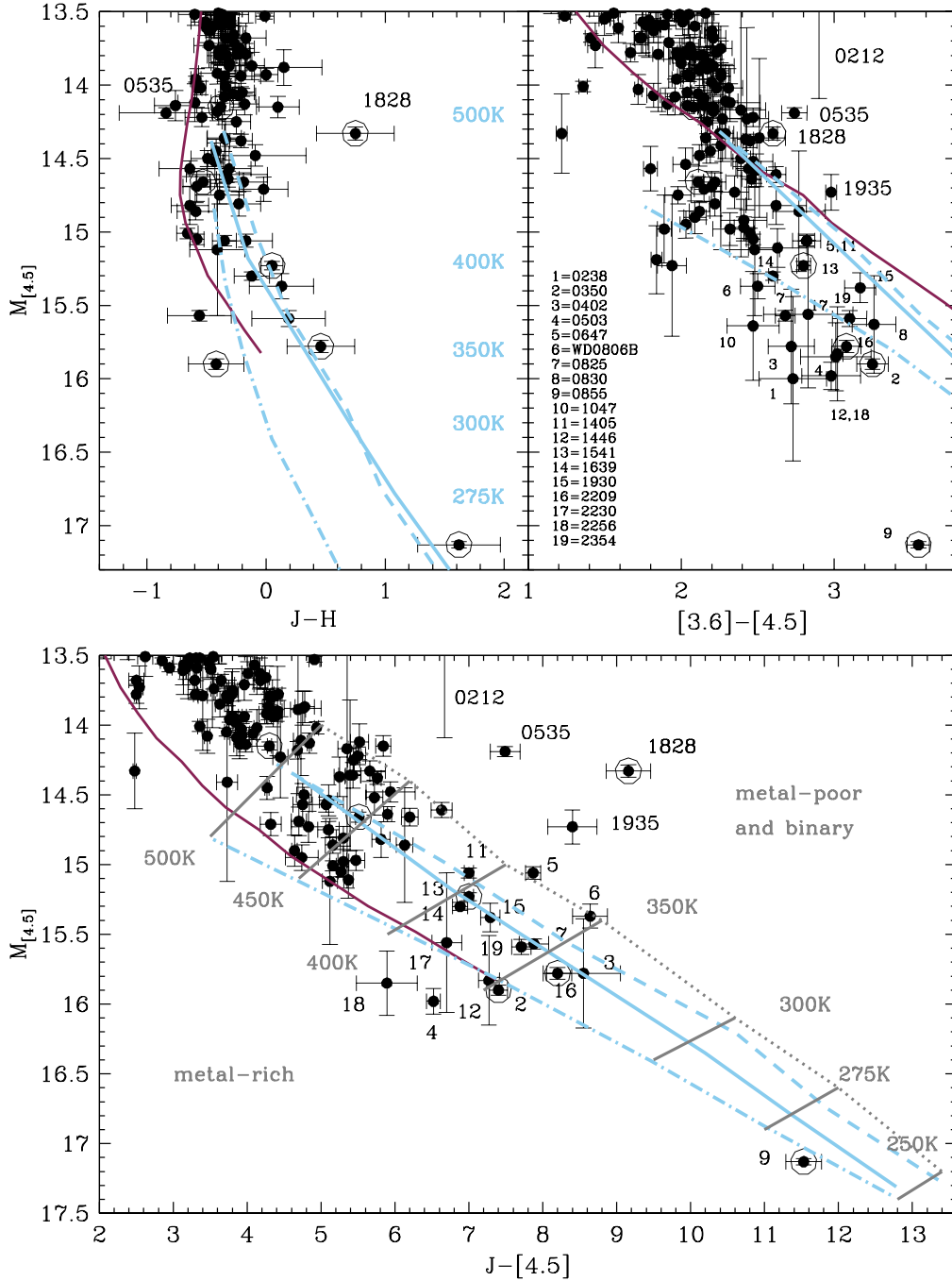
into the  $\text{NH}_3$  form from  $\text{N}_2$ , in equilibrium conditions (Figure 7). It is interesting to note that our fits indicate that the  $P - T$  curve reverts to the standard adiabat at pressures around 10 bar for the 325–475 K Y dwarfs in our sample, and 50 bar for the 260 K J0855; all at temperatures of 750–870 K (the very metal-poor J1828(AB) system appears to transition at a slightly cooler 640 K). This may indicate that convection in Y dwarf atmospheres is disrupted once the atmosphere cools to  $\sim 800$  K, by the change in nitrogen chemistry and/or the condensation of chlorides and sulfides. We find that for the warmer T9 dwarf J0722 any increase in  $\gamma$  occurs at higher pressures, which are not sampled by the emergent SED, suggesting different physics is at play for T dwarfs.

#### 5.4. $5\,\mu\text{m}$ Spectra of Brown Dwarfs and the Detection of Phosphine

Phosphine is a nonequilibrium species that is seen in the  $5\,\mu\text{m}$  spectra of Saturn and Jupiter; it is a useful species that can be used to study both atmospheric dynamics and the effect of photochemistry on planetary atmospheres (e.g., Fletcher et al. 2009).  $\text{PH}_3$  is not detected in ground-based spectra of J0855 and other cold brown dwarfs, although it is expected to be abundant (Skemer et al. 2016; Morley et al. 2018; Miles et al. 2020). Because of the potential diagnostic value of the species, we explore what the new tuned models indicate for its detectability.

Figure 10(a) shows  $3.5\text{--}5.5\,\mu\text{m}$  spectra of the four brown dwarfs in our tuning sample with such data. We also show the



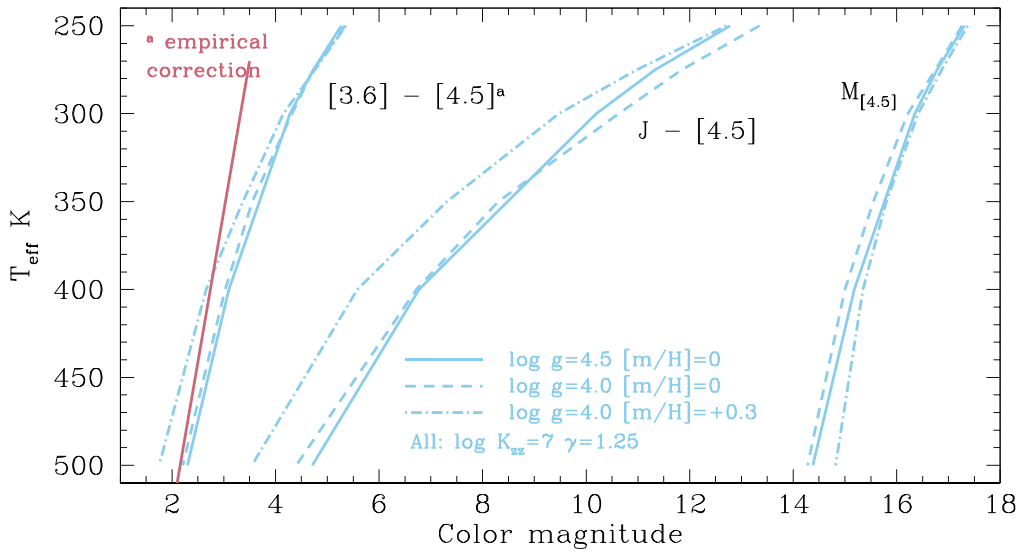


**Figure 13.** Color-magnitude diagrams for late-T and Y dwarfs. Sequences are as in Figure 12. Gray ~diagonal lines in the bottom panel indicate constant  $T_{\text{eff}}$ , as labeled, for metallicities ranging from approximately +0.3 on the left, to -0.5 on the right. The location of the metal-poor envelope edge in the bottom panel is consistent with the low-metallicity Sonora-Bobcat models (Figure 3), and with the observed population. Our SED analysis of J1828 indicates that it is an equal-mass binary with the low-metallicity J0212, J0535, and J1935 are also likely to be similar-mass binary systems. Notionally single Y dwarfs which are estimated to have  $T_{\text{eff}} \lesssim 400$  K are identified in the legend by the first four digits of the WISE catalog R.A., or their binary name in the case of the white dwarf companion.

derived adiabat-tuned fit for each object, which reproduces the observations well. Figure 10(b), (c) show the opacity contributions from various species at these wavelengths, for representative temperatures. These opacity contributions are taken from the ATMO 2020 models with vertical mixing, which only consider the nonequilibrium abundances of the major carbon- and nitrogen-bearing species, and thus do not take into account the mixing of  $\text{PH}_3$  (Phillips et al. 2020).

The spectral regions that can be observed from the ground, the  $L$  and  $M$  bands, are dominated by  $\text{CH}_4$  and  $\text{CO}$  absorption

bands, respectively, for the 400 K and warmer brown dwarfs. For the 260 K J0855,  $\text{H}_2\text{O}$  becomes the dominant opacity source in the  $M$  band. Although (Morley et al. 2018, their Figure 19) find that the red edge of the  $L$  band and the blue edge of the  $M$  band in J0855 should show  $\text{PH}_3$  absorption, at the enhanced abundance brought about by mixing, these are difficult wavelengths to work at from ground-based observatories. We calculate that there is a strong feature due to  $\text{PH}_3$  at  $4.30 \mu\text{m}$  in the spectra of cold brown dwarfs, even when assuming  $\text{PH}_3$  is in chemical equilibrium. Hence, JWST



**Figure 14.** Synthetic colors from the modified-adiabat model grid; see the text. Table 4 gives polynomial fits to the solar metallicity relationships shown in the Figure.

**Table 4**  
Polynomial Relationships for Estimating  $T_{\text{eff}}$  from Color

Color	$a_0$	$a_1$	$a_2$
$[3.6] - [4.5]^a$	850	-166.7	
$J - [4.5]$	816	-81.64	2.9572
$M_{[4.5]}$	5331	-544.5	14.4990

**Note.**  $T_{\text{eff}}$  is estimated using:  $T_{\text{eff}} = a_0 + a_1 \times \text{Color} + a_2 \times \text{Color}^2$ . Relationships are valid for  $250 \leq T_{\text{eff}} \leq 500$  K. Excluding any systematic errors, the uncertainty in  $T_{\text{eff}}$  is  $\pm 25$  K. Solar metallicity is assumed; metal-rich objects will be cooler, and metal-poor object warmer, for a given  $J - [4.5]$  (see Table 5 and Figure 14).

<sup>a</sup> Semiempirical.

**Table 5**  
Estimate of Color Sensitivity to Metallicity and Gravity for  $T_{\text{eff}} = 400$  K

Color	$\delta \text{ mag}$		Important Chemistry
	$\delta \log g = +0.5$	$\delta [\text{m}/\text{H}] = +0.3$	
$\delta(J - H)$	-0.1	-0.3	$\text{H}_2$ at $J$
$\delta(J - K)$	-0.7	+0.4	(stronger) $\text{H}_2$ at $K$
$\delta(J - [4.5])$	+0.1	-1.1	$\text{H}_2$ at $J$ , CO at $[4.5]$
$\delta([3.6] - [4.5])$	-0.2	+0.4	$\text{CH}_4$ at $[3.6]$ , CO at $[4.5]$
$\delta([4.5] - \text{W}3)$	-0.2	+0.6	CO at $[4.5]$ , $\text{H}_2$ at W3

**Note.** Generated by a  $P - T$  modified-adiabat model with  $K_{\text{zz}} = 10^7 \text{ cm}^2 \text{ s}^{-1}$ ,  $\gamma = 1.25$  and  $P_{\gamma\text{-max}} = 15$  bar, except for the  $[3.6] - [4.5]$  color, which is empirical. See also Figure 5 for opacity identification and Figure 6 for SED sensitivity to gravity and metallicity.

observations should finally confirm the presence of  $\text{PH}_3$  in brown dwarf atmospheres.

### 5.5. Estimating Masses and Ages for the Six Y Dwarfs

Figure 11 shows the evolution of cold brown dwarfs in a  $T_{\text{eff}}$ :gravity diagram. The luminosity, or absolute brightness, of a brown dwarf, as measured at the Earth, is determined by  $T_{\text{eff}}$ , radius and distance. The uncertainty in distance is very small

for these nearby objects, and the SED is very sensitive to temperature (Figure 6), with the net result that the absolute flux level constrains radius to  $\sim 10\%$  (Figures 8 and 9). Figure 11 shows that  $\log g$  can then be constrained to  $\pm 0.3$  dex, mass can be constrained to a factor of  $\sim 2$ , and age to a factor of  $\sim 3$ , for a notional 400 K brown dwarf.

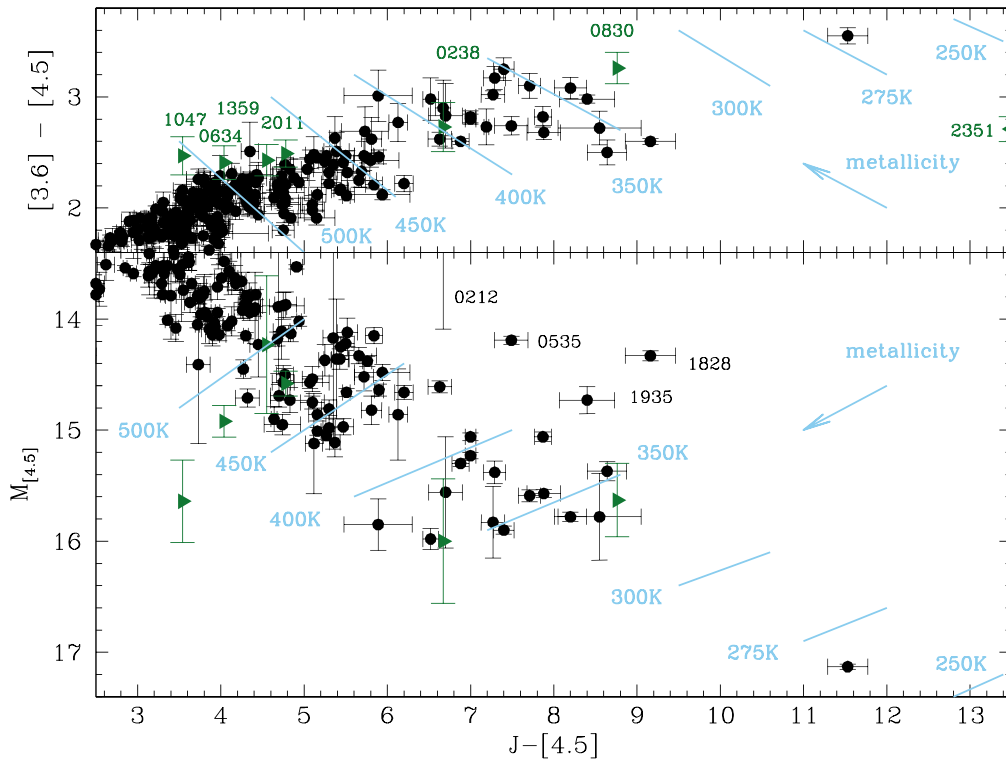
Table 3 gives the atmospheric and evolutionary parameters we derived here from the  $T_{\text{eff}}$  and gravity of each tuned-adiabat model fit. For our tuning sample of six Y dwarfs, the evolutionary models give ages of between approximately 0.5 and 3 Gyr (Table 3, see also Figure 11). These values agree, within the uncertainties, with what would be expected for a local sample, 1–3 Gyr (Dupuy & Liu 2017; Buder et al. 2019). Weak support for relative youth is provided by the tangential velocities which suggest thin disk membership (Dupuy & Liu 2012) and so an age younger than 8 Gyr (Kilic et al. 2017). The estimated masses for the six Y dwarfs are very low for this cold sample—between 5 and 12 Jupiters.

## 6. Application to the Larger Y Dwarf Sample

### 6.1. Color Trends

To check how the modified-adiabat nonequilibrium chemistry models perform for a larger sample, Figures 12 and 13 repeat the color–color and color–magnitude diagrams of Figures 2 and 3, but this time they include a model sequence generated by a small grid of the  $P - T$ -modified models. For this grid we adopt  $K_{\text{zz}} = 10^7 \text{ cm}^2 \text{ s}^{-1}$ ,  $\gamma = 1.25$ , and  $P_{\gamma\text{-max}} = 15$  bar. Colors are calculated for two gravities,  $\log g = 4.0$  and  $4.5$ , and two metallicities,  $[\text{m}/\text{H}] = 0.0$  and  $+0.3$ . A sequence generated by the standard nonequilibrium chemistry model is also shown for comparison.

The top panel of Figure 12,  $J - [4.5]: Y - J$ , shows that there is a systematic issue in the  $Y$  band for the 325–450 K brown dwarfs, as the models are fainter at  $Y$  than observed, by a few-tenths to one magnitude. The spectral fits in Figures 8 and 9 suggest that the problem is too little flux in the models at the blue wing of the  $Y$  band, suggesting in turn that a more rigorous approach to the treatment of the strong  $0.8 \mu\text{m}$  K I line is called for (see Section 4). The models are likely to have issues with two important chemical changes at 325–450 K, exploration of



**Figure 15.** Color-color plots for estimating  $T_{\text{eff}}$  and metallicity for Y dwarfs. Blue lines are isotherms with metallicity ranging from approximately +0.3 to −0.5 from left to right. Green triangles, identified in the upper panel with the first four digits of the object’s R.A., correspond to candidate Y dwarfs with lower limits only on  $J$ , or no constraint on  $J$  in the case of J2351. In the lower panel, the possible equal-mass binaries J0212, J0535, J1828, and J1935 are identified. Of the seven  $J$ -limit objects, J2351 is not in the lower panel as there is no parallax available.

which are beyond the scope of this paper: collisions with  $\text{H}_2$  affect the shape of the wings of the alkali resonance lines (Allard et al. 2016), and neutral K gas transitions to KCl gas and then to KCl solid (e.g., Lodders 1999).

The fits to the other colors and magnitudes in Figures 12 and 13 are good to excellent. The agreement between the models and observations at  $J - K$  and  $[3.6] - [4.5]$  is greatly improved. The previous  $\gtrsim 1$  magnitude discrepancy for these colors is now  $\approx 0$  for  $J - K$  and reduced to a few-tenths of a magnitude for  $[3.6] - [4.5]$ . In the color-magnitude diagram, Figure 13, the previous  $\approx 0.4$  mag discrepancy in  $J - H$  is resolved, as is the  $\approx 1.0$  mag discrepancy in  $J - [4.5]$ .

## 6.2. $T_{\text{eff}}$ and Metallicity Estimates for Y Dwarfs

Figures 12 and 13 show that, as well as temperature, the metallicity, and gravity of the atmosphere can impact the colors of a brown dwarf. We find that temperature and metallicity have the largest impact, as also indicated by the synthetic spectra shown in Figure 6.

Figure 14 is a plot of  $T_{\text{eff}}$  against  $[3.6] - [4.5]$ ,  $J - [4.5]$ , and  $M_{[4.5]}$ , which are the most commonly available photometric measurements for Y dwarfs, currently. The relationships in Figure 14 are determined from the modified-adiabat model grid, which spans  $250 \leq T_{\text{eff}} \text{ K} \leq 500$ . These models have  $K_{\text{zz}} = 10^7 \text{ cm}^2 \text{ s}^{-1}$ ,  $\gamma = 1.25$  and  $P_{\gamma\text{-max}} = 15$  bar. The relationship for the  $[3.6] - [4.5]$  color includes an empirical correction based on observations of the Y dwarfs for which we do a full SED fit in Section 5.2. The Figure suggests that the  $J - [4.5]$  color is particularly sensitive to metallicity. Table 4 gives polynomial fits to the solar metallicity relationships shown in Figure 14. We

estimate the uncertainty in a color-derived  $T_{\text{eff}}$  to be  $\pm 25$  K, based on the scatter seen when determining  $T_{\text{eff}}$  from different colors, and comparing the SED-determined  $T_{\text{eff}}$  to the color value.

Table 5 summarizes the dependencies of various colors on metallicity and gravity for a representative 400 K brown dwarf. All color changes are calculated by a modified-adiabat model, except for  $[3.6] - [4.5]$  which is estimated from the two 375 K brown dwarfs analyzed in Section 5, which differ in metallicity and gravity. By referencing the SED parameter dependence shown in Figure 6, and the opacity identifications shown in Figure 5, we find that there are two opacities which drive the pressure (gravity) and metallicity sensitivity in the models: the CO absorption at  $\lambda \approx 4.6 \mu\text{m}$  (Figure 6), and collision-induced  $\text{H}_2$  opacity (e.g., Allard & Hauschildt 1995; Burgasser et al. 2002; Knapp et al. 2004; Saumon et al. 2012). The  $\text{H}_2$  opacity at these low temperatures has two broad peaks with similar absorption coefficients, at  $\lambda \approx 2.2 \mu\text{m}$  ( $K$ ) and  $\lambda \approx 11.1 \mu\text{m}$  ( $W3$ ); there is a weaker absorption peak at  $\lambda \approx 1.2 \mu\text{m}$  ( $YJ$ , Saumon et al. 2012, their Figure 1).

Figure 15 shows late-T and Y dwarf candidates in color-color diagrams which take advantage of the metallicity sensitivity of the  $J - [4.5]$  color, which becomes redder with decreasing metallicity. For warmer brown dwarfs, Schneider et al. (2020, their Figure 3) show that metal-poor T-type (sub) dwarfs are also red in  $J - [4.5]$  for their  $W1 - W2$  color, which is similar to the  $[3.6] - [4.5]$  color. Note that the observationally defined metal-poor population edge, in the lower panels of Figures 13 and 15, is consistent with the location of the metal-poor chemical-equilibrium Sonora-Bobcat sequence shown in Figure 3. This would be expected, as metal

**Table 6**  
Estimates of  $T_{\text{eff}}$  and Metallicity for Candidate and Confirmed Y Dwarfs

WISE Name	Discovery Ref.	Spec. Type	Type Ref.	$T_{\text{eff}}$ K	[m/H]	WISE Name	Discovery Ref.	Spec. Type	Type Ref.	$T_{\text{eff}}$ K	[m/H]
014656.66+423410.0B <sup>a</sup>	Ki12	Y0	Du15	435	~0	120604.38+840110.6	Sc15	Y0	Sc15	475	~0
021243.55+053147.2(AB) <sup>b,c</sup>	Me20a	Y1	1	400		121756.91+162640.2B	Ki11	Y0	Le14	460	~0
023842.60-133210.7	Me20a	Y1	Me20a	400		125721.01+715349.3	Me20b	Y1	Me20b	390	~0
030237.53-581740.3	Ti18	Y0:	Ti18	460	>0	135937.65-435226.9 <sup>c</sup>	Me20a	Y0	Me20a	455	
030449.03-270508.3	Pi14b	Y0pec	Pi14a	465	~0	140518.40+553421.4	Cu11	Y0.5	Cu16	400	~0
032109.59+693204.5	Me20a	Y0.5	Me20a	415	>0	144606.62-231717.8	Me20a	Y1	Me20a	350	>0
033605.05-014350.4	Ma13b	Y0	Ma18	445	<0	154151.66-225025.2 <sup>d</sup>	Cu11	Y1	Sc15	375	+0.3
035000.32-565830.2 <sup>d</sup>	Ki12	Y1	Ki12	325	+0.3	163940.86-684744.6	Ti12	Y0pec	Sc15	405	~0
035934.06-540154.6	Ki12	Y0	Ki12	475	<0	173835.53+273258.9	Cu11	Y0	Cu11	450	>0
040235.55-265145.4	Me20a	Y1	Me20a	370	<0	182831.08+265037.8(AB) <sup>d,e</sup>	Cu11	≥Y2	Ki12	375	-0.5
041022.71+150248.5	Cu11	Y0	Cu11	435	>0	193054.55-205949.4	Me20b	Y1	Me20b	365	~0
050305.68-564834.0	Me20b	Y1	Me20b	345	>0	193518.59-154620.3(AB) <sup>e</sup>	Me20a	Y1	Me20a	365	<0
053516.80-750024.9(AB) <sup>c</sup>	Ki12	≥Y1:	Ki13	415	<0	193656.08+040801.2	Me20a	Y0	Me20a	450	~0
063428.10+504925.9	Me20a	Y0	Me20a	445		201146.45-481259.7	Me20a	Y0	Me20a	465	
064723.23-623235.5	Ki13	Y1	Ki13	405	<0	205628.90+145953.3 <sup>d</sup>	Cu11	Y0	Cu11	475	0.0
071322.55-291751.9	Ki12	Y0	Ki12	465	~0	220905.73+271143.9 <sup>d</sup>	Cu14	Y0:	Cu14	350	0.0
073444.02-715744.0	Ki12	Y1	Ki12	470	~0	222055.31-362817.4	Ki12	Y0	Ki12	450	~0
080714.68-661848.7	Lu11	Y1	Ki19	415	<0	223022.60+254907.5 <sup>c</sup>	Me20a	Y1	Me20a	395	
082507.35+280548.5	Sc15	Y0.5	Sc15	380	~0	224319.56-145857.3	Me20b	Y0	Me20b	450	
083011.95+283716.0	Ba20	Y1	Ba20	335		225628.97+400227.3	Me20a	Y1	Me20a	345	>0
085510.83-071442.5 <sup>d</sup>	Lu14	≥Y4	Ki19	260	0.0	235120.62-700025.8	Me20b	Y0.5	1	405	
085938.95+534908.7 <sup>c</sup>	Me20a	Y0	Me20a	450		235402.79+024014.1	Sc15	Y0	Sc15	355	~0
093852.89+063440.6 <sup>c</sup>	Me20a	Y0	Me20a	455		235547.99+380438.9	Me20a	Y0	Me20a	480	
094005.50+523359.2 <sup>c</sup>	Me20a	≥Y1	Me20a	410		235644.78-481456.3	Me20a	Y0.5	Me20a	425	
104756.81+545741.6	Me20a	Y0	Me20a	400							
114156.67-332635.5	Ti18	Y0	Ti18	485	~0						

#### Notes.

<sup>a</sup> No measured resolved 5  $\mu\text{m}$  photometry is published for the close binary. For this work we deconvolve the Spitzer photometry (Kirkpatrick et al. 2019) using spectral types of T9 and Y0 for the components (Dupuy et al. 2015), and adopting  $\delta[3.6] = 1.00 \pm 0.15$  and  $\delta[4.5] = 0.7 \pm 0.10$  (Kirkpatrick et al. 2021, their Figure 14).

<sup>b</sup>  $T_{\text{eff}}$  is estimated from  $[3.6] - [4.5]$  and  $J - [4.5]$ ; the value is consistent with the  $M_{[4.5]}$ -implied value if the system is an equal-mass binary and the true parallax is close to the upper limit on the current uncertain measurement.

<sup>c</sup> The  $M_{[4.5]}$  magnitude was ignored in the estimate due to the large uncertainty in the distance modulus ( $>0.4$  mag).

<sup>d</sup> The parameter estimates are based on the full SED fits described in Section 5.2.

<sup>e</sup> The parameter estimates assume the system is an equal-mass binary.

**References.** (1) this work, type ( $\pm 0.5$ ) based on the type-color relationship of Kirkpatrick et al. (2019), Ba20—Bardalez Gagliuffi et al. (2020), Cu11—Cushing et al. (2011), Du15—Dupuy et al. (2015), Ki11, 12, 13, 19—Kirkpatrick et al. (2011, 2012, 2013, 2019), Le14—Leggett et al. (2014), Lu11, 14—Luhman et al. (2011); Luhman (2014), Ma13b—Mace et al. (2013a), Ma18—Martin et al. (2018), Ma19—Marocco et al. 2019, Me20a,b—Meisner et al. (2020a), Meisner2020b; Pi14a—Pinfield et al. (2014b), Sc15—Schneider et al. (2015), Ti12, 14, 18—Tinney et al. (2012, 2014, 2018).

paucity reduces the size of the chemical changes brought about by mixing (Zahnle & Marley 2014, their Figures 4 and 10).

The commonly available colors for Y dwarfs are shown in Figure 15:  $[3.6] - [4.5]$  and  $M_{[4.5]}$  as a function of  $J - [4.5]$ . Observations, together with the modified-adiabat disequilibrium chemistry models (with an empirical correction to  $[3.6] - [4.5]$ ), show that  $T_{\text{eff}}$  and metallicity can be estimated for cold brown dwarfs using such a figure.

Figure 15 includes all 50 currently known candidate Y dwarfs. Seven of these do not have a measurement of  $J$ . A lower limit of  $J \gtrsim 24.6$  was determined for WISEA J083011.95+283716.0 by transforming the F125W limit given by Bardalez Gagliuffi et al. (2020) using transformations from Leggett et al. (2017). Lower limits on  $J$  were taken from Meisner et al. (2020a, 2020b) for CWISEP J104756.81+545741.6 ( $J \gtrsim 19.8$ ) and CWISEP J201146.45-481259.7 ( $J \gtrsim 20.1$ ). For three other objects we determined limits from the UKIDSS and VISTA surveys'

imaging data: CWISEP J023842.60-133210.7 ( $J \gtrsim 23.0$ ), CWISEP J063428.10+504925.9 ( $J \gtrsim 20.0$ ), and CWISEP J135937.65-435226.9 ( $J \gtrsim 20.5$ ). No constraint on  $J$  is currently available for WISEA J235120.62-700025.8.

Table 6 lists the 50 Y dwarfs (or Y dwarf candidates) along with spectral type,  $T_{\text{eff}}$  and (where there is sufficient information) [m/H]. For six of the Y dwarfs, identified in the Table, we carried out a detailed atmospheric analysis in Section 5.2, and those values of  $T_{\text{eff}}$  and [m/H] are given in the Table, as well as in Table 3. The parameters for the other Y dwarfs are based on one to three colors, using the relationships given in Table 4.  $T_{\text{eff}}$  is determined from  $[3.6] - [4.5]$ ,  $J - [4.5]$  and  $M_{[4.5]}$ , with the  $T_{\text{eff}}$  values rounded to 5 K. The average of the color-implied  $T_{\text{eff}}$  value is adopted, unless all three estimates are available and the  $J - [4.5]$  color is discrepant (suggesting a non-solar metallicity, Figures 14 and 15), in which case the two other values are averaged.



**Table 7**  
Known and Candidate Binary Y Dwarfs

WISE (Other) Name	Separation			Mass Ratio	
	arcsecond	au <sup>a</sup>	Ref.	Value	Ref.
014656.66+423410.0B	0.09''	1.7	Du15	0.9	Du15
021243.55+053147.2(AB)	< 0.36''	< 9	1	1.0	1
053516.80–750024.9(AB)	< 0.15''	< 2.2	Op16	1.0	1
080714–661848 (WD 0806–661B)	130	2500	Lu11	0.004 <sup>b</sup>	Lu11
121756.91+162640.2B	0.76''	7.1	Li12	0.7	Le14
182831.08+265037.8(AB)	< 0.05''	< 0.4	Be13	1.0	1
193518.59–154620.3(AB)	< 0.35''	< 5	1	1.0	1

**Notes.**

<sup>a</sup> Distance in astronomical unit calculated using parallaxes from Kirkpatrick et al. (2021). For J0212 the upper limit on the parallax is used, which is more consistent with the observed colors (Figures 3, 13, 15).

<sup>b</sup> The mass ratio uses the white dwarf progenitor mass.

**References.** (1) this work; Be13—Beichman et al. (2013), Du15—Dupuy et al. (2015), Le14—Leggett et al. (2014), Li12—Liu et al. (2012), Lu11—Luhman et al. (2011), Op16—Opitz et al. (2016).

### 6.3. Super-luminous Y Dwarfs and Binarity

There are four Y dwarfs for which the luminosity-implied  $T_{\text{eff}}$  is only consistent with the SED- or color-implied value if the dwarf is an unresolved multiple system: CWISEP J021243.55+053147.2, WISE J053516.80–750024.9, WISEPA J182831.08+265037.8, and CWISEP J193518.59–154620.3 (see Figures 3, 13, and 15).

If these four objects are approximately equal-mass binaries, the sample of 50 Y dwarf systems then includes the secondaries of three known resolved systems, plus these four unresolved binaries, for a notional binary fraction of 14%. Table 7 summarizes the properties of these confirmed and candidate binaries. The number of candidate binary systems is consistent with studies of the binary fraction of substellar objects—for example Fontanive et al. (2018) find a binary fraction of  $8\% \pm 6\%$  for T5–Y0 brown dwarfs at separations of 1.0–1000 au, with a mass ratio distribution peaking around unity.

## 7. Conclusions

The cold Y dwarfs are important laboratories for atmospheric dynamics because the regions from which the 1–10  $\mu\text{m}$  light emerges span a range in pressure of 3 orders of magnitude (Figure 7). They are also rapid rotators (Cushing et al. 2016; Esplin et al. 2016; Leggett et al. 2016b; Tannock et al. 2021). Under these conditions, small departures from standard radiative/convective equilibrium is a natural and stable phenomenon (e.g., Guillot 2005; Augustson & Mathis 2019; Tremblin et al. 2019; Zhang 2020). In this work we show that a  $\sim 10\%$  reduction in the standard adiabat in the upper photosphere of Y dwarfs leads to cooler deeper photospheres. This change yields significant and comprehensive improvements in the agreement between modeled and observed colors and spectra of brown dwarfs with  $T_{\text{eff}} < 600$  K (Figures 5, 12, 13). The modified-adiabat models with nonequilibrium chemistry that we outline here produce the best fit to date of the 1–20  $\mu\text{m}$  flux distribution of brown dwarfs cooler than 600 K (Figures 5, 8, 9). A summary of key results follows.

1. New near-infrared photometry is presented for four late-T and 17 Y dwarfs (Table 1).
2. New or revised mid-infrared photometry is presented for one L, 10 T, and four Y dwarfs (Table 2).
3. Spectral type estimates are revised in Section 2 for three brown dwarfs, using the new photometry:
  - (a) CWISEP 021243.55+053147.2 from background source to likely binary Y dwarf system
  - (b) CWISE J092503.20–472013. from Y0 to T8
  - (c) CWISE J112106.36–623221.5 from Y0 to T7
4. We reconfirm that chemical abundances are not in equilibrium, due to vertical mixing (Figures 2, 3, 5). The decrease in  $\text{NH}_3$  and increase in CO impacts the flux at  $H$ ,  $K$ , [4.5] and  $W3$  by 30% to a factor of two. Of particular importance for JWST, chemical equilibrium models will underestimate the [4.5] –  $W3$  ( $\sim 14 \mu\text{m}$ ) and [4.5] –  $W4$  ( $\sim 22 \mu\text{m}$ ) colors of T and Y dwarfs by  $\sim 1$  magnitude (Figure 4).
5. Current (2020) atmospheric models generate  $J - K$  and [3.6] – [4.5] colors that deviate from observations by a factor of  $\sim 3$ , for  $T_{\text{eff}} < 600$  K (Figure 2).
6. As a first step toward including processes currently missing in all brown dwarf models, we parameterize the pressure-temperature atmospheric profile in the one-dimensional ATMO 2020 disequilibrium chemistry models, and explore fits to the SEDs of seven brown dwarfs with  $260 \lesssim T_{\text{eff}}$  K  $\lesssim 540$  K (Section 5). A decrease in the adiabatic gradient at pressures of 10–50 bar and temperatures  $\sim 800$  K produces cooler deep atmospheres for a given  $T_{\text{eff}}$ , and effectively reproduces observations at  $1 \lesssim \lambda \mu\text{m} \lesssim 20$  (Figures 5, 8, 9). Discrepancies that remain are at the factor of  $\sim 2$  level in the  $Y$  and [3.6] bands for  $T_{\text{eff}} \lesssim 400$  K (Figure 12). Note that the discrepancy at [3.6] is reduced by a factor of  $\sim 5$  compared to standard-adiabat models.
7. Spectroscopy shows that the problems at  $Y$  and [3.6] for the  $T_{\text{eff}} \lesssim 400$  K Y dwarfs occur at the blue side of the passbands.
  - (a) For  $Y$ , the issue is most likely to be deficiencies in modeling the red wing of the  $\text{KI}$  resonant line (Phillips et al. 2020).
  - (b) For [3.6], it appears that high in the atmosphere, where pressures are  $\sim 0.1$  bar and this flux originates, the temperature needs to be higher. The heating could be caused by breaking gravity waves, as is likely in the solar system giant planet atmospheres above the 1 bar pressure surface (e.g., Schubert et al. 2003; O’Donoghue et al. 2016). The  $T_{\text{eff}} \lesssim 350$  K Y dwarfs may have an upper atmosphere heated by water condensation (Figure 7).
8. The fact that the adiabat changes at temperatures around 800 K and pressures of 10–50 bar, for the six Y dwarfs studied in detail, may indicate that convection is disrupted in Y dwarf atmospheres by a change in nitrogen chemistry and/or the condensation of chlorides and sulfides (Figure 7, top left panel).
9. The atmospheric parameters combined with evolutionary models indicate that the six Y dwarfs have an age between 0.5 and 3 Gyr and masses of 5–12 Jupiters (Table 3).
10. We generate a limited grid of modified-adiabat disequilibrium chemistry models and provide relationships between  $T_{\text{eff}}$  and the commonly used colors: [3.6] – [4.5],  $J - [4.5]$ , and  $M_{[4.5]}$  (Table 4). The models indicate

that there are two opacities which drive the pressure (gravity) and metallicity sensitivity in the models: the CO absorption at  $\lambda \approx 4.6 \mu\text{m}$  (Figure 6), and collision-induced  $\text{H}_2$  opacity with broad peaks at  $\lambda \approx 1.2, 2.2$ , and  $11.1 \mu\text{m}$  (Saumon et al. 2012, their Figure 1).

11. We show that the  $J - [4.5]$  color is particularly sensitive to metallicity (Table 5), and that a diagram, which plots  $[3.6] - [4.5]$  and  $M_{[4.5]}$  as a function of  $J - [4.5]$ , can be used to estimate  $T_{\text{eff}}$  and metallicity (Figure 15). We estimate these parameters for the 50 known candidate Y dwarfs (Table 6).
12. We find that there are four super-luminous Y dwarfs which are likely to be unresolved binaries; together with the three known resolved binary Y dwarf components, this suggests a binary fraction of  $\sim 14\%$  for Y dwarfs (Table 7). Such a number is consistent with what is found for L and T dwarfs (e.g., Fontanive et al. 2018).
13. The Appendices give examples of temperature-sensitive JWST colors (Appendix A), tables of colors generated by the modified-adiabat model grid (Appendix B), and a compilation of the photometry used in this work (Appendix C).

Supported by the international Gemini Observatory, a program of NSF's NOIRLab, which is managed by the Association of Universities for Research in Astronomy (AURA) under a cooperative agreement with the National Science Foundation, on behalf of the Gemini partnership of Argentina, Brazil, Canada, Chile, the Republic of Korea, and the United States of America.

This work was enabled in part by observations made from the Gemini North Telescope, located within the Maunakea Science

Reserve and adjacent to the summit of Maunakea. We are grateful for the privilege of observing the universe from a place that is unique in both its astronomical quality and its cultural significance.

This publication makes use of data products from the Wide-field Infrared Survey Explorer, which is a joint project of the University of California, Los Angeles, and the Jet Propulsion Laboratory/California Institute of Technology, funded by the National Aeronautics and Space Administration.

This work is based in part on observations made with the Spitzer Space Telescope, obtained from the NASA/ IPAC Infrared Science Archive, both of which are operated by the Jet Propulsion Laboratory, California Institute of Technology under a contract with the National Aeronautics and Space Administration.

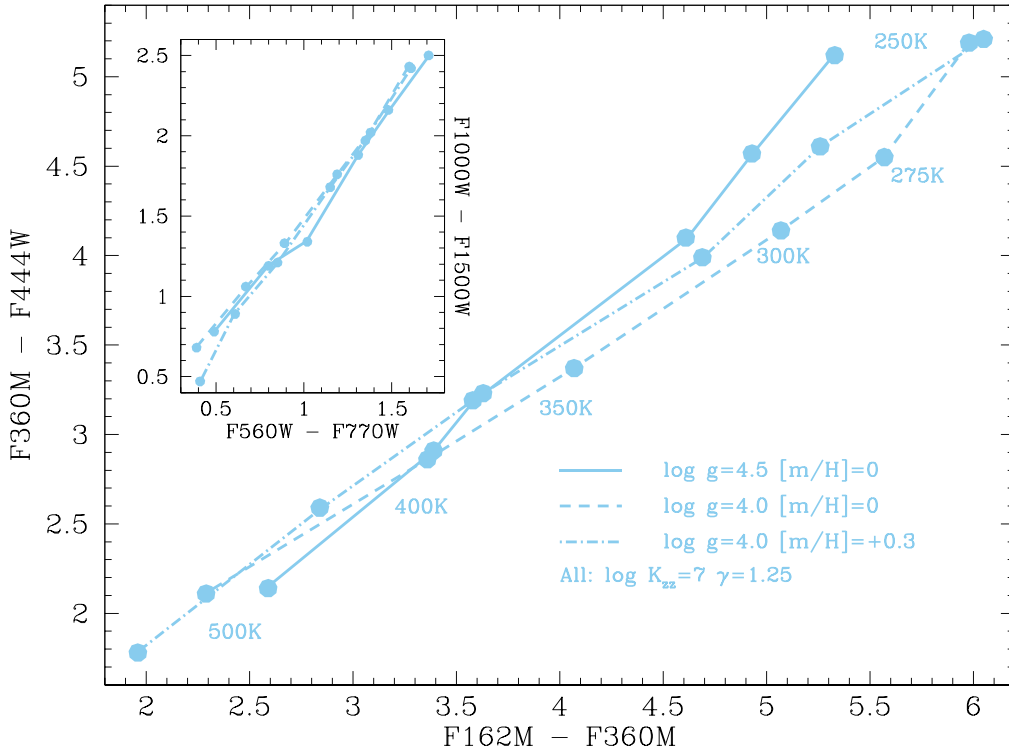
C.V.M. acknowledges the support of the National Science Foundation grant number 1910969.

P.T. acknowledges supports by the European Research Council under Grant Agreement ATMO 757858.

*We dedicate this work to France Allard and Adam Showman, both prematurely lost to astronomy in 2020. They leave a legacy of work that is vital to the understanding of low-mass stars, brown dwarfs, exoplanets, and the solar system.*

## Appendix A JWST Colors

Figure 16 shows color-color diagrams for JWST NIRCam and MIRI, generated by the same small grid of modified-adiabat models, for  $250 \leq T_{\text{eff}} \text{ K} \leq 500$ . We chose the color combinations shown in the figure based on sensitivity to  $T_{\text{eff}}$  and measurability. The latter was determined from the model-calculated brightness of the brown dwarf and the throughput of



**Figure 16.** Blue lines are color-color sequences generated by the grid of modified-adiabat models for JWST filters. The atmospheric parameters are given in the legend. Dots along each sequence indicate where  $T_{\text{eff}} = 500, 400, 350, 300, 275$ , and  $250 \text{ K}$ , from left to right. The large diagram is for NIRCam and the inset for MIRI. The colors were chosen for sensitivity to  $T_{\text{eff}}$  (based on the models) and measurability (based on the brightness of the brown dwarf and the throughput of the filters).

the NIRCам<sup>23</sup> and MIRI<sup>24</sup> filters. We found, for example, that the best short-wavelength filter in NIRCам for cold brown dwarf work is the F162M. The shorter wavelength filters either sample regions where there is very little signal (F 070W, F 090W, F 140M) or are wide enough to include a significant wavelength region with no signal (F 115W, F 150W). We give the JWST magnitudes in Table 9 and the reader can explore other color combinations. The modified-adiabat models we present here indicate that JWST colors can be used to estimate brown dwarf temperatures, and vice versa; this is especially true at shorter wavelengths, as can also be seen in the top left panel of Figure 6.

## Appendix B Model Grid

Tables 8 and 9 give colors generated by the modified-adiabat ATMO 2020 disequilibrium chemistry model atmospheres. The models have  $K_{zz} = 10^7 \text{ cm}^2 \text{ s}^{-1}$ ,  $\gamma = 1.25$  and  $P_{\gamma-\text{max}} = 15 \text{ bar}$ . Table 8 gives magnitudes on the MKO near-infrared system, as well as Spitzer [3.6] and [4.5], and WISE W3 and W4. Table 9 gives magnitudes for a subset of the JWST filters, those which are likely to be used for observations of brown dwarfs.

**Table 8**  
ATMO 2020 Grid with Modified  $P - T$  Profile: MKO, Spitzer, and WISE Filters

$T_{\text{eff}}$ K	$\log g$	[m/H]	$Y$	$J$	$H$	$K$	[3.6]	[4.5]	W3	W4
250	4.0	0.0	32.02	30.61	29.21	31.27	22.60	17.26	15.05	12.95
275	4.0	0.0	29.79	28.60	27.63	28.94	21.48	16.75	14.56	12.70
300	4.0	0.0	27.94	26.83	26.15	27.10	20.53	16.21	14.08	12.42
350	4.0	0.0	24.86	23.85	23.67	24.16	19.10	15.55	13.39	12.08
400	4.0	0.0	22.78	21.72	21.81	21.97	18.03	15.00	12.84	11.80
500	4.0	0.0	19.77	18.68	19.05	18.92	16.49	14.28	12.04	11.38
250	4.5	0.0	30.66	30.09	28.54	31.85	22.58	17.31	15.24	13.11
275	4.5	0.0	28.71	28.11	27.03	29.61	21.51	16.78	14.80	12.87
300	4.5	0.0	27.17	26.54	25.80	27.75	20.63	16.35	14.39	12.66
350	4.5	0.0	24.77	23.57	23.28	24.80	19.20	15.86	13.63	12.31
400	4.5	0.0	22.80	21.95	22.10	22.90	18.28	15.18	13.25	12.09
500	4.5	0.0	20.16	19.09	19.55	19.73	16.68	14.38	12.41	11.66
250	4.0	0.3	31.50	30.08	29.42	29.89	22.73	17.37	14.87	12.90
275	4.0	0.3	29.14	27.85	27.50	27.74	21.63	16.87	14.40	12.69
300	4.0	0.3	27.12	25.88	25.83	25.75	20.56	16.41	13.90	12.38
350	4.0	0.3	24.22	23.11	23.31	23.02	19.17	15.80	13.20	12.06
400	4.0	0.3	22.07	20.93	21.27	20.82	18.01	15.35	12.63	11.77
500	4.0	0.3	19.48	18.36	18.80	18.27	16.57	14.82	11.94	11.38

**Note.** All models have  $\gamma = 1.25$  and  $\log K_{zz} = 7.0$ . Magnitudes are for a distance of 10 pc and are on the Vega system.

<sup>23</sup> <https://jwst-docs.stsci.edu/near-infrared-camera/nircam-observing-modes/nircam-imaging>

<sup>24</sup> <https://jwst-docs.stsci.edu/mid-infrared-instrument/miri-predicted-performance/miri-sensitivity>

**Table 9**  
ATMO 2020 Grid with Modified  $P - T$  Profile: JWST Filters

$T_{\text{eff}}$ K	$\log g$	[m/H]	NIRCam F									MIRI F							
			115W	150W	162M	200W	210M	300M	360M	410M	444W	560W	770W	1000W	1280W	1500W	1800W	2100W	2550W
250	4.0	0.0	31.16	29.56	28.65	31.72	30.81	26.36	22.67	18.61	17.48	19.21	17.61	16.22	14.57	13.79	13.32	13.01	12.86
275	4.0	0.0	29.12	27.98	27.08	29.38	28.47	24.64	21.51	17.89	16.96	18.39	17.02	15.43	14.10	13.41	12.99	12.75	12.64
300	4.0	0.0	27.34	26.51	25.61	27.52	26.62	23.25	20.54	17.19	16.41	17.67	16.48	14.77	13.63	13.01	12.63	12.45	12.36
350	4.0	0.0	24.34	24.03	23.15	24.54	23.66	21.03	19.08	16.24	15.71	16.57	15.68	13.80	12.97	12.47	12.18	12.09	12.04
400	4.0	0.0	22.23	22.17	21.34	22.31	21.45	19.47	17.98	15.45	15.12	15.71	15.03	13.10	12.42	12.04	11.83	11.80	11.76
500	4.0	0.3	19.21	19.42	18.71	19.19	18.37	17.37	16.42	14.31	14.30	14.45	14.06	12.12	11.60	11.44	11.32	11.36	11.34
250	4.5	0.0	30.61	28.89	27.98	32.23	31.40	26.52	22.65	18.52	17.53	19.47	17.76	16.46	14.76	13.96	13.49	13.18	13.02
275	4.5	0.0	28.61	27.39	26.48	29.99	29.15	24.99	21.55	17.85	16.98	18.68	17.20	15.76	14.33	13.60	13.17	12.92	12.79
300	4.5	0.0	27.01	26.16	25.25	28.15	27.29	23.69	20.64	17.28	16.54	18.00	16.69	15.16	13.95	13.28	12.89	12.69	12.59
350	4.5	0.0	24.16	23.64	22.76	25.14	24.31	21.25	19.18	16.35	15.99	16.87	15.85	14.05	13.21	12.71	12.43	12.33	12.26
400	4.5	0.0	22.44	22.47	21.61	23.25	22.41	20.12	18.22	15.67	15.31	16.13	15.33	13.58	12.84	12.39	12.15	12.09	12.05
500	4.5	0.0	19.63	19.93	19.17	20.03	19.22	17.88	16.58	14.51	14.44	14.80	14.30	12.54	12.00	11.76	11.62	11.64	11.61
250	4.0	0.3	30.56	29.77	28.86	30.41	29.44	26.16	22.81	18.62	17.59	19.19	17.58	16.01	14.40	13.59	13.17	12.94	12.85
275	4.0	0.3	28.31	27.86	26.95	28.23	27.27	24.42	21.69	17.92	17.08	18.37	17.03	15.21	13.93	13.24	12.87	12.71	12.65
300	4.0	0.3	26.35	26.19	25.29	26.23	25.27	22.95	20.59	17.45	16.60	17.58	16.44	14.52	13.46	12.84	12.50	12.39	12.35
350	4.0	0.3	23.57	23.67	22.80	23.44	22.51	20.70	19.17	16.31	15.93	16.51	15.66	13.53	12.76	12.32	12.07	12.05	12.04
400	4.0	0.3	21.42	21.63	20.83	21.19	20.28	19.11	17.99	15.51	15.40	15.60	15.00	12.80	12.18	11.91	11.73	11.75	11.75
500	4.0	0.3	18.87	19.15	18.47	18.58	17.71	17.25	16.51	14.50	14.73	14.48	14.07	11.94	11.47	11.47	11.29	11.35	11.34

**Note.** All models have  $\gamma = 1.25$  and  $\log K_{\text{zz}} = 7.0$ . Magnitudes are for a distance of 10 pc and are on the Vega system.

## Appendix C

### Photometry Compilation

Table 10 presents a compilation of the photometry used in this work.

**Table 10**  
Compilation of Measurements for T6 and Later Brown Dwarfs


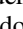
Survey Name	Discovery R.A. Decl.		Sp. Type	$M - m$	$Y$	$J$	$H$	$K$	$L'$	[3.6]	[4.5]	W1	W2	W3 mag	$e_{Mn}$	$e_Y$	$e_J$	$e_H$	$e_K$	$e_{L'}$	$e_{3.6}$	$e_{4.5}$	$e_{W1}$	$e_{W2}$	$e_{W3}$	References				
	hhmmss.ss	± ddmss.s																								Discovery	Sp. Type	Parallax	Near-IR	Spitzer
CWISEP	000229.93	+635217.0	7.5							17.35	15.69															Meisner_2020b	Meisner_2020b			Meisner_2020b
WISE	000517.48	+373720.5	9.0	0.52	18.48	17.59	17.98	17.99	14.43	15.43	13.28	16.76	13.29	11.79	0.04	0.02	0.02	0.03	0.03	0.10	0.04	0.04	0.09	0.03	0.24	Mace_2013a	Mace_2013a	Kirkpatrick_2019	Leggett_2015	Kirkpatrick_2019
CWISEP	001146.07	-471306.8	8.5			19.28	19.69			17.74	15.81	18.94	15.99			0.07	0.20				0.09	0.02	0.27	0.06		Meisner_2020a	Meisner_2020a		VISTA_VHS	Meisner_2020a
WISE	001354.39	+063448.2	8.0		20.56	19.54	19.98	20.79		17.15	15.16		15.23			0.04	0.03	0.04	0.10		0.03	0.03		0.09		Pinfield_2014a	Pinfield_2014a		Leggett_2015	Pinfield_2014a
WISEA	001449.96	+795116.1	8.0		20.32	19.36				17.76	15.88	18.72	16.00	13.69		0.10	0.10				0.04	0.02	0.28	0.06	0.40	Bardalez_2020	Bardalez_2020		this_work	Bardalez_2020

**References.** (1) this work; Albert\_2011—Albert et al. (2011), Artigau\_2010—Artigau et al. (2010), Bardalez\_2020—Bardalez Gagliuffi et al. (2020), Best\_2015—Best et al. (2015), Best\_2020—Best et al. (2020), Burgasser\_1999—Burgasser et al. (1999), Burgasser\_2000—Burgasser et al. (2000), Burgasser\_2002—Burgasser et al. (2002), Burgasser\_2003—Burgasser et al. (2003), Burgasser\_2004—Burgasser et al. (2004), Burgasser\_2006—Burgasser et al. (2006), Burgasser\_2008—Burgasser et al. (2008), Burningham\_2008—Burningham et al. (2008), Burningham\_2009—Burningham et al. (2009), Burningham\_2010a—Burningham et al. (2010), Burningham\_2010b—Burningham et al. (2010), Burningham\_2011—Burningham et al. (2011), Burningham\_2013—Burningham et al. (2013), Chiu\_2006—Chiu et al. (2006), Cushing\_2011—Cushing et al. (2011), Cushing\_2014—Cushing et al. (2014), Cushing\_2016—Cushing et al. (2016), Delorme\_2008—Delorme et al. (2008), Delorme\_2010—Delorme et al. (2010), Dupuy\_2012—Dupuy & Liu (2012), Dupuy\_2013—Dupuy & Kraus (2013), Dupuy\_2015—Dupuy et al. (2015), Faherty\_2012—Faherty et al. (2012), Faherty\_2020—Faherty et al. (2020), GAIA—Gaia Collaboration et al. (2018), Gelino\_2011—Gelino et al. (2011), Goldman\_2010—Goldman et al. (2010), Greco\_2019—Greco et al. (2019), Griffith\_2012—Griffith et al. (2012), Kirkpatrick\_2011—Kirkpatrick et al. (2011), Kirkpatrick\_2012—Kirkpatrick et al. (2012), Kirkpatrick\_2013—Kirkpatrick et al. (2013), Kirkpatrick\_2019—Kirkpatrick et al. (2019), Kirkpatrick\_2021—Kirkpatrick et al. (2021), Knapp\_2004—Knapp et al. (2004), Leggett\_2002—Leggett et al. (2002), Leggett\_2009—Leggett et al. (2009), Leggett\_2010—Leggett et al. (2010), Leggett\_2012—Leggett et al. (2012), Leggett\_2014—Leggett et al. (2014), Leggett\_2015—Leggett et al. (2015), Leggett\_2017—Leggett et al. (2017), Leggett\_2019—Leggett et al. (2019), Liu\_2011—Liu et al. (2011), Liu\_2012—Liu et al. (2012), Lodieu\_2007—Lodieu et al. (2007), Lodieu\_2009—Lodieu et al. (2009), Lodieu\_2012—Lodieu et al. (2012), Looper\_2007—Looper et al. (2007), Lucas\_2010—Lucas et al. (2010), Luhman\_2011—Luhman et al. (2011), Luhman\_2012—Luhman et al. (2012), Luhman\_2014—Luhman (2014), Mace\_2013a—Mace et al. (2013b), Mace\_2013b—Mace et al. (2013a), Mainzer\_2011—Mainzer et al. (2011), Manjavacas\_2013—Manjavacas et al. (2013), Morocco\_2010—Morocco et al. (2010), Morocco\_2020—Morocco et al. (2020), Martin\_2018—Martin et al. (2018), Meisner\_2020a—Meisner et al. (2020a), Meisner\_2020b—Meisner et al. (2020b), Murray\_2011—Murray et al. (2011), Patten\_2006—Patten et al. (2006), Pinfield\_Gromadzki\_2014—Pinfield, P. and Gromadzki, M. private communication 2014; Pinfield\_2008—Pinfield et al. (2008), Pinfield\_2012—Pinfield et al. (2012), Pinfield\_2014a—Pinfield et al. (2014a), Pinfield\_2014b—Pinfield et al. (2014b), Scholz\_2010a—Scholz (2010a), Scholz\_2010b—Scholz (2010b), Scholz\_2011—Scholz et al. (2011), Smart\_2010—Smart et al. (2010), Strauss\_2009—Strauss et al. (2009), Stephens\_2004—Stephens & Leggett (2004), Subasavage\_2009—Subasavage et al. (2009), Thompson\_2013—Thompson et al. (2013), Tinney\_2003—Tinney et al. (2003), Tinney\_2005—Tinney et al. (2005), Tinney\_2012—Tinney et al. (2012), Tinney\_2014—Tinney et al. (2014), Tinney\_2018—Tinney et al. (2018), Tsvetanov\_2000—Tsvetanov et al. (2000), Vrba\_2004—Vrba et al. (2004), Warren\_2007—Warren et al. (2007), Wright\_2013—Wright et al. (2013).

(This table is available in its entirety in machine-readable form.)



## ORCID iDs

S. K. Leggett  <https://orcid.org/0000-0002-3681-2989>  
 Pascal Tremblin  <https://orcid.org/0000-0001-6172-3403>  
 Mark W. Phillips  <https://orcid.org/0000-0001-6041-7092>  
 Trent J. Dupuy  <https://orcid.org/0000-0001-9823-1445>  
 Mark Marley  <https://orcid.org/0000-0002-5251-2943>  
 Caroline Morley  <https://orcid.org/0000-0002-4404-0456>  
 Adam Schneider  <https://orcid.org/0000-0002-6294-5937>  
 Sarah E. Logsdon  <https://orcid.org/0000-0002-9632-9382>

## References

- Ackerman, A. S., & Marley, M. S. 2001, *ApJ*, **556**, 872  
 Albert, L., Artigau, É., Delorme, P., et al. 2011, *AJ*, **141**, 203  
 Allard, F., & Hauschildt, P. H. 1995, *ApJ*, **445**, 433  
 Allard, N. F., Spiegelman, F., & Kielkopf, J. F. 2016, *A&A*, **589**, A21  
 Apai, D., Karalidi, T., Marley, M. S., et al. 2017, *Sci*, **357**, 683  
 Artigau, É., Radigan, J., Folkes, S., et al. 2010, *ApJL*, **718**, L38  
 Augustson, K. C., & Mathis, S. 2019, *ApJ*, **874**, 83  
 Baraffe, I., Chabrier, G., Allard, F., & Hauschildt, P. H. 1998, *A&A*, **337**, 403  
 Bardalez Gagliuffi, D. C., Faherty, J. K., Schneider, A. C., et al. 2020, *ApJ*, **895**, 145  
 Beichman, C., Gelino, C. R., Kirkpatrick, J. D., et al. 2013, *ApJ*, **764**, 101  
 Best, W. M. J., Liu, M. C., Dupuy, T. J., & Magnier, E. A. 2017, *ApJL*, **843**, L4  
 Best, W. M. J., Liu, M. C., Magnier, E. A., et al. 2015, *ApJ*, **814**, 118  
 Best, W. M. J., Liu, M. C., Magnier, E. A., & Dupuy, T. J. 2020, *AJ*, **159**, 257  
 Bowler, B. P., Blunt, S. C., & Nielsen, E. L. 2020, *AJ*, **159**, 63  
 Buder, S., Lind, K., Ness, M. K., et al. 2019, *A&A*, **624**, A19  
 Burgasser, A. J., Geballe, T. R., Leggett, S. K., Kirkpatrick, J. D., & Golimowski, D. A. 2006, *ApJ*, **637**, 1067  
 Burgasser, A. J., Kirkpatrick, J. D., Brown, M. E., et al. 1999, *ApJL*, **522**, L65  
 Burgasser, A. J., Kirkpatrick, J. D., Brown, M. E., et al. 2002, *ApJ*, **564**, 421  
 Burgasser, A. J., Kirkpatrick, J. D., Cutri, R. M., et al. 2000, *ApJL*, **531**, L57  
 Burgasser, A. J., McElwain, M. W., & Kirkpatrick, J. D. 2003, *AJ*, **126**, 2487  
 Burgasser, A. J., McElwain, M. W., Kirkpatrick, J. D., et al. 2004, *AJ*, **127**, 2856  
 Burgasser, A. J., Tinney, C. G., Cushing, M. C., et al. 2008, *ApJL*, **689**, L53  
 Burningham, B., Cardoso, C. V., Smith, L., et al. 2013, *MNRAS*, **433**, 457  
 Burningham, B., Leggett, S. K., Lucas, P. W., et al. 2010, *MNRAS*, **404**, 1952  
 Burningham, B., Lucas, P. W., Leggett, S. K., et al. 2011, *MNRAS*, **414**, L90  
 Burningham, B., Marley, M. S., Line, M. R., et al. 2017, *MNRAS*, **470**, 1177  
 Burningham, B., Pinfield, D. J., Leggett, S. K., et al. 2008, *MNRAS*, **391**, 320  
 Burningham, B., Pinfield, D. J., Leggett, S. K., et al. 2009, *MNRAS*, **395**, 1237  
 Burningham, B., Pinfield, D. J., Lucas, P. W., et al. 2010, *MNRAS*, **406**, 1885  
 Burrows, A., & Liebert, J. 1993, *RvMP*, **65**, 301  
 Burrows, A., Marley, M., Hubbard, W. B., et al. 1997, *ApJ*, **491**, 856  
 Burrows, A., & Sharp, C. M. 1999, *ApJ*, **512**, 843  
 Chabrier, G., Mazevet, S., & Soubiran, F. 2019, *ApJ*, **872**, 51  
 Chiu, K., Fan, X., Leggett, S. K., et al. 2006, *AJ*, **131**, 2722  
 Cushing, M. C., Hardegree-Ullman, K. K., Trucks, J. L., et al. 2016, *ApJ*, **823**, 152  
 Cushing, M. C., Kirkpatrick, J. D., Gelino, C. R., et al. 2011, *ApJ*, **743**, 50  
 Cushing, M. C., Kirkpatrick, J. D., Gelino, C. R., et al. 2014, *AJ*, **147**, 113  
 Cushing, M. C., Rayner, J. T., Davis, S. P., & Vacca, W. D. 2003, *ApJ*, **582**, 1066  
 Cushing, M. C., Rayner, J. T., & Vacca, W. D. 2005, *ApJ*, **623**, 1115  
 Cushing, M. C., Schneider, A. C., Kirkpatrick, J. D., et al. 2021, arXiv:2107.00506  
 Dantona, F., & Mazzitelli, I. 1985, *ApJ*, **296**, 502  
 Delorme, P., Albert, L., Forveille, T., et al. 2010, *A&A*, **518**, A39  
 Delorme, P., Delfosse, X., Albert, L., et al. 2008, *A&A*, **482**, 961  
 Dupuy, T. J., & Kraus, A. L. 2013, *Sci*, **341**, 1492  
 Dupuy, T. J., & Liu, M. C. 2012, *ApJS*, **201**, 19  
 Dupuy, T. J., & Liu, M. C. 2017, *ApJS*, **231**, 15  
 Dupuy, T. J., Liu, M. C., & Leggett, S. K. 2015, *ApJ*, **803**, 102  
 Dye, S., Lawrence, A., Read, M. A., et al. 2018, *MNRAS*, **473**, 5113  
 Eikenberry, S., Elston, R., Raines, S. N., et al. 2006, *Proc. SPIE*, **6269**, 626917  
 Esplin, T. L., & Luhman, K. L. 2017, *AJ*, **154**, 134  
 Esplin, T. L., Luhman, K. L., Cushing, M. C., et al. 2016, *ApJ*, **832**, 58  
 Faherty, J. K., Burgasser, A. J., Walter, F. M., et al. 2012, *ApJ*, **752**, 56  
 Faherty, J. K., Goodman, S., Caselden, D., et al. 2020, *ApJ*, **889**, 176  
 Fazio, G. G., Hora, J. L., Allen, L. E., et al. 2004, *ApJS*, **154**, 10  
 Fegley, B., & Prinn, R. G. 1985, *ApJ*, **299**, 1067  
 Filippazzo, J. C., Rice, E. L., Faherty, J., et al. 2015, *ApJ*, **810**, 158  
 Flasar, F. M., & Gierasch, P. J. 1978, *GAFFD*, **10**, 175  
 Fletcher, L. N., Orton, G. S., Teanby, N. A., & Irwin, P. G. J. 2009, *Icar*, **202**, 543  
 Fontanive, C., Biller, B., Bonavita, M., & Allers, K. 2018, *MNRAS*, **479**, 2702  
 Gaia Collaboration, Brown, A. G. A., Vallenari, A., et al. 2018, *A&A*, **616**, A1  
 Geballe, T. R., Knapp, G. R., Leggett, S. K., et al. 2002, *ApJ*, **564**, 466  
 Gelino, C. R., Kirkpatrick, J. D., Cushing, M. C., et al. 2011, *AJ*, **142**, 57  
 Goldman, B., Marsat, S., Henning, T., Clemens, C., & Greiner, J. 2010, *MNRAS*, **405**, 1140  
 Gonzales, E., Burningham, B., Faherty, J., et al. 2020, arXiv:2010.01224  
 Greco, J. J., Schneider, A. C., Cushing, M. C., Kirkpatrick, J. D., & Burgasser, A. J. 2019, *AJ*, **158**, 182  
 Griffith, R. L., Kirkpatrick, J. D., Eisenhardt, P. R. M., et al. 2012, *AJ*, **144**, 148  
 Guillot, T. 2005, *AREPS*, **33**, 493  
 Guillot, T., Chabrier, G., Morel, P., & Gautier, D. 1994, *Icar*, **112**, 354  
 Hodapp, K. W., Jensen, J. B., Irwin, E. M., et al. 2003, *PASP*, **115**, 1388  
 Kesseli, A. Y., Kirkpatrick, J. D., Fajardo-Acosta, S. B., et al. 2019, *AJ*, **157**, 63  
 Kilic, M., Munn, J. A., Harris, H. C., et al. 2017, *ApJ*, **837**, 162  
 Kirkpatrick, J. D., Cushing, M. C., Gelino, C. R., et al. 2011, *ApJS*, **197**, 19  
 Kirkpatrick, J. D., Cushing, M. C., Gelino, C. R., et al. 2013, *ApJ*, **776**, 128  
 Kirkpatrick, J. D., Gelino, C. R., Cushing, M. C., et al. 2012, *ApJ*, **753**, 156  
 Kirkpatrick, J. D., Gelino, C. R., Faherty, J. K., et al. 2021, *ApJS*, **253**, 7  
 Kirkpatrick, J. D., Martin, E. C., Smart, R. L., et al. 2019, *ApJS*, **240**, 19  
 Knapp, G. R., Leggett, S. K., Fan, X., et al. 2004, *AJ*, **127**, 3553  
 Labrie, K., Anderson, K., Cárdenas, R., Simpson, C., & Turner, J. E. H. 2019, in ASP Conf. Ser. 523, DRAGONS—Data Reduction for Astronomy from Gemini Observatory North and South, ed. P. J. Teuben et al. (San Francisco, CA: ASP), 321  
 Lawrence, A., Warren, S. J., Almaini, O., et al. 2007, *MNRAS*, **379**, 1599  
 Leggett, S. K., Burningham, B., Saumon, D., et al. 2010, *ApJ*, **710**, 1627  
 Leggett, S. K., Currie, M. J., Varricatt, W. P., et al. 2006, *MNRAS*, **373**, 781  
 Leggett, S. K., Cushing, M. C., Hardegree-Ullman, K. K., et al. 2016b, *ApJ*, **830**, 141  
 Leggett, S. K., Cushing, M. C., Saumon, D., et al. 2009, *ApJ*, **695**, 1517  
 Leggett, S. K., Dupuy, T. J., Morley, C. V., et al. 2019, *ApJ*, **882**, 117  
 Leggett, S. K., Golimowski, D. A., Fan, X., et al. 2002, *ApJ*, **564**, 452  
 Leggett, S. K., Liu, M. C., Dupuy, T. J., et al. 2014, *ApJ*, **780**, 62  
 Leggett, S. K., Morley, C. V., Marley, M. S., et al. 2013, *ApJ*, **763**, 130  
 Leggett, S. K., Morley, C. V., Marley, M. S., & Saumon, D. 2015, *ApJ*, **799**, 37  
 Leggett, S. K., Saumon, D., Marley, M. S., et al. 2007, *ApJ*, **655**, 1079  
 Leggett, S. K., Saumon, D., Marley, M. S., et al. 2012, *ApJ*, **748**, 74  
 Leggett, S. K., Tremblin, P., Esplin, T. L., Luhman, K. L., & Morley, C. V. 2017, *ApJ*, **842**, 118  
 Leggett, S. K., Tremblin, P., Saumon, D., et al. 2016a, *ApJ*, **824**, 2  
 Line, M. R., Marley, M. S., Liu, M. C., et al. 2017, *ApJ*, **848**, 83  
 Line, M. R., Teske, J., Burningham, B., Fortney, J. J., & Marley, M. S. 2015, *ApJ*, **807**, 183  
 Liu, M. C., Delorme, P., Dupuy, T. J., et al. 2011, *ApJ*, **740**, 108  
 Liu, M. C., Dupuy, T. J., Bowler, B. P., Leggett, S. K., & Best, W. M. J. 2012, *ApJ*, **758**, 57  
 Lodders, K. 1999, *ApJ*, **519**, 793  
 Lodieu, N., Burningham, B., Day-Jones, A., et al. 2012, *A&A*, **548**, A53  
 Lodieu, N., Burningham, B., Hambly, N. C., & Pinfield, D. J. 2009, *MNRAS*, **397**, 258  
 Lodieu, N., Hambly, N. C., & Cross, N. J. G. 2021, *MNRAS*, **503**, 2265  
 Lodieu, N., Pinfield, D. J., Leggett, S. K., et al. 2007, *MNRAS*, **379**, 1423  
 Looper, D. L., Kirkpatrick, J. D., & Burgasser, A. J. 2007, *AJ*, **134**, 1162  
 Lucas, P. W., Tinney, C. G., Burningham, B., et al. 2010, *MNRAS*, **408**, L56  
 Luhman, K. L. 2014, *ApJL*, **786**, L18  
 Luhman, K. L., Burgasser, A. J., & Bochanski, J. J. 2011, *ApJL*, **730**, L9  
 Luhman, K. L., Burgasser, A. J., Labbé, I., et al. 2012, *ApJ*, **744**, 135  
 Luhman, K. L., & Esplin, T. L. 2016, *AJ*, **152**, 78  
 Luhman, K. L., & Hapich, C. J. 2020, *AJ*, **160**, 57  
 Mace, G. N., Kirkpatrick, J. D., Cushing, M. C., et al. 2013a, *ApJ*, **777**, 36  
 Mace, G. N., Kirkpatrick, J. D., Cushing, M. C., et al. 2013b, *ApJS*, **205**, 6  
 Mainzer, A., Cushing, M. C., Skrutskie, M., et al. 2011, *ApJ*, **726**, 30  
 Manjavacas, E., Goldman, B., Reffert, S., & Henning, T. 2013, *A&A*, **560**, A52  
 Marley, M., & Robinson, T. 2015, *ARA&A*, **53**, 279  
 Marley, M. S., Saumon, D., Fortney, J. J., et al. 2017, AAS Meeting, **230**, 315.07

- Marley, M. S., Saumon, D., Visscher, C., et al. 2021, arXiv:2107.07434
- Marocco, F., Caselden, D., Meisner, A. M., et al. 2019, *ApJ*, **881**, 17
- Marocco, F., Kirkpatrick, J. D., Meisner, A. M., et al. 2020, *ApJL*, **888**, L19
- Marocco, F., Smart, R. L., Jones, H. R. A., et al. 2010, *A&A*, **524**, A38
- Martin, E. C., Kirkpatrick, J. D., Beichman, C. A., et al. 2018, *ApJ*, **867**, 109
- McGregor, P., Hart, J., Stevanovic, D., et al. 2004, *Proc. SPIE*, **5492**, 1033
- McMahon, R. G., Banerji, M., Gonzalez, E., et al. 2013, *Msngr*, **154**, 35
- Meisner, A. M., Caselden, D., Kirkpatrick, J. D., et al. 2020a, *ApJ*, **889**, 74
- Meisner, A. M., Faherty, J. K., Kirkpatrick, J. D., et al. 2020b, *ApJ*, **899**, 123
- Miles, B. E., Skemer, A. J. I., Morley, C. V., et al. 2020, *ApJ*, **160**, 63
- Morley, C. V., Fortney, J. J., Marley, M. S., et al. 2012, *ApJ*, **756**, 172
- Morley, C. V., Marley, M. S., Fortney, J. J., et al. 2014, *ApJ*, **787**, 78
- Morley, C. V., Skemer, A. J., Allers, K. N., et al. 2018, *ApJ*, **858**, 97
- Murray, D. N., Burningham, B., Jones, H. R. A., et al. 2011, *MNRAS*, **414**, 575
- Nielsen, E. L., De Rosa, R. J., Macintosh, B., et al. 2019, *AJ*, **158**, 13
- Nikutta, R., Hunt-Walker, N., Nenkova, M., Ivezić, Ž., & Elitzur, M. 2014, *MNRAS*, **442**, 3361
- Noll, K. S., Geballe, T. R., & Marley, M. S. 1997, *ApJL*, **489**, L87
- O'Donoghue, J., Moore, L., Stallard, T. S., & Melin, H. 2016, *Natur*, **536**, 190
- Opitz, D., Tinney, C. G., Faherty, J. K., et al. 2016, *ApJ*, **819**, 17
- Patten, B. M., Stauffer, J. R., Burrows, A., et al. 2006, *ApJ*, **651**, 502
- Phillips, M. W., Tremblin, P., Baraffe, I., et al. 2020, *A&A*, **637**, A38
- Piette, A. A. A., & Madhusudhan, N. 2020, *MNRAS*, **497**, 5136
- Pinfield, D. J., Burningham, B., Lodieu, N., et al. 2012, *MNRAS*, **422**, 1922
- Pinfield, D. J., Burningham, B., Tamura, M., et al. 2008, *MNRAS*, **390**, 304
- Pinfield, D. J., Gomes, J., Day-Jones, A. C., et al. 2014a, *MNRAS*, **437**, 1009
- Pinfield, D. J., Gromadzki, M., Leggett, S. K., et al. 2014b, *MNRAS*, **444**, 1931
- Robinson, T. D., & Catling, D. C. 2012, *ApJ*, **757**, 104
- Ruiz, M. T., Leggett, S. K., & Allard, F. 1997, *ApJL*, **491**, L107
- Saumon, D., Chabrier, G., & van Horn, H. M. 1995, *ApJS*, **99**, 713
- Saumon, D., Geballe, T. R., Leggett, S. K., et al. 2000, *ApJ*, **541**, 374
- Saumon, D., & Marley, M. S. 2008, *ApJ*, **689**, 1327
- Saumon, D., Marley, M. S., Abel, M., Frommhold, L., & Freedman, R. S. 2012, *ApJ*, **750**, 74
- Saumon, D., Marley, M. S., Cushing, M. C., et al. 2006, *ApJ*, **647**, 552
- Saumon, D., Marley, M. S., Leggett, S. K., et al. 2007, *ApJ*, **656**, 1136
- Schlaufman, K. C. 2018, *ApJ*, **853**, 37
- Schneider, A. C., Burgasser, A. J., Gerasimov, R., et al. 2020, *ApJ*, **898**, 77
- Schneider, A. C., Cushing, M. C., Kirkpatrick, J. D., et al. 2015, *ApJ*, **804**, 92
- Scholz, A., Moore, K., Jayawardhana, R., et al. 2018, *ApJ*, **859**, 153
- Scholz, R. D. 2010a, *A&A*, **510**, L8
- Scholz, R. D. 2010b, *A&A*, **515**, A92
- Scholz, R. D., Bihain, G., Schnurr, O., & Storm, J. 2011, *A&A*, **532**, L5
- Schubert, G., Hickey, M. P., & Walterscheid, R. L. 2003, *Icar*, **163**, 398
- Showman, A. P., & Kaspi, Y. 2013, *ApJ*, **776**, 85
- Showman, A. P., Tan, X., & Zhang, X. 2019, *ApJ*, **883**, 4
- Skemer, A. J., Morley, C. V., Allers, K. N., et al. 2016, *ApJL*, **826**, L17
- Smart, R. L., Jones, H. R. A., Lattanzi, M. G., et al. 2010, *A&A*, **511**, A30
- Stephens, D. C., & Leggett, S. K. 2004, *PASP*, **116**, 9
- Strauss, M. A., Fan, X., Gunn, J. E., et al. 1999, *ApJL*, **522**, L61
- Subasavage, J. P., Jao, W.-C., Henry, T. J., et al. 2009, *AJ*, **137**, 4547
- Sutherland, W., Emerson, J., Dalton, G., et al. 2015, *A&A*, **575**, A25
- Tannock, M. E., Metchev, S., Heinze, A., et al. 2021, *AJ*, **161**, 224
- Tennyson, J., Harris, G. J., Barber, R. J., et al. 2007, *MolPh*, **105**, 701
- Thompson, M. A., Kirkpatrick, J. D., Mace, G. N., et al. 2013, *PASP*, **125**, 809
- Tinney, C. G., Burgasser, A. J., & Kirkpatrick, J. D. 2003, *AJ*, **126**, 975
- Tinney, C. G., Burgasser, A. J., Kirkpatrick, J. D., & McElwain, M. W. 2005, *AJ*, **130**, 2326
- Tinney, C. G., Faherty, J. K., Kirkpatrick, J. D., et al. 2012, *ApJ*, **759**, 60
- Tinney, C. G., Faherty, J. K., Kirkpatrick, J. D., et al. 2014, *ApJ*, **796**, 39
- Tinney, C. G., Kirkpatrick, J. D., Faherty, J. K., et al. 2018, *ApJS*, **236**, 28
- Tokunaga, A. T., Simons, D. A., & Vacca, W. D. 2002, *PASP*, **114**, 180
- Tremblin, P., Amundsen, D. S., Mourier, P., et al. 2015, *ApJL*, **804**, L17
- Tremblin, P., Padiou, T., Phillips, M. W., et al. 2019, *ApJ*, **876**, 144
- Tsuji, T., Ohnaka, K., & Aoki, W. 1996, *A&A*, **305**, L1
- Tsvetanov, Z. I., Golimowski, D. A., Zheng, W., et al. 2000, *ApJL*, **531**, L61
- Vazan, A., & Helled, R. 2020, *A&A*, **633**, A50
- Visscher, C., & Moses, J. I. 2011, *ApJ*, **738**, 72
- Visscher, C., Moses, J. I., & Saslow, S. A. 2010, *Icar*, **209**, 602
- Vos, J. M., Allers, K. N., & Biller, B. A. 2017, *ApJ*, **842**, 78
- Vos, J. M., Biller, B. A., Allers, K. N., et al. 2020, *ApJ*, **160**, 38
- Vrba, F. J., Henden, A. A., Luginbuhl, C. B., et al. 2004, *AJ*, **127**, 2948
- Wagner, K., Apai, D., & Kratter, K. M. 2019, *ApJ*, **877**, 46
- Wang, D., Lunine, J. I., & Mousis, O. 2016, *Icar*, **276**, 21
- Warren, S. J., Mortlock, D. J., Leggett, S. K., et al. 2007, *MNRAS*, **381**, 1400
- Werner, M. W., Roellig, T. L., Low, F. J., et al. 2004, *ApJS*, **154**, 1
- Woitke, P., & Helling, C. 2003, *A&A*, **399**, 297
- Wright, E. L., Eisenhardt, P. R. M., Mainzer, A. K., et al. 2010, *AJ*, **140**, 1868
- Wright, E. L., Mainzer, A., Kirkpatrick, J. D., et al. 2014, *AJ*, **148**, 82
- Wright, E. L., Skrutskie, M. F., Kirkpatrick, J. D., et al. 2013, *AJ*, **145**, 84
- Zahnle, K. J., & Marley, M. S. 2014, *ApJ*, **797**, 41
- Zalesky, J. A., Line, M. R., Schneider, A. C., & Patience, J. 2019, *ApJ*, **877**, 24
- Zapatero Osorio, M. R., Martín, E. L., Bouy, H., et al. 2006, *ApJ*, **647**, 1405
- Zhang, X. 2020, *RAA*, **20**, 099